INTERIM REPORT

Advanced SAS Imaging Methods for Resonating Underwater Acoustic Targets

SERDP Project MR-2322

APRIL 2014

Ira Ekhaus
Peter B. Weichman
BAE Systems

Distribution Statement A
This document has been cleared for public release

SERDP
DOD ▪ EPA ▪ DOE

Interim Report: Advanced SAS Imaging Methods for Resonating Underwater Acoustic Targets

Ira Ekhaus and Peter B. Weichman
BAE Systems, Technology Solutions, 6 New England Executive Place, Burlington, MA 01803
(Dated: April 7, 2014)

This document presents a detailed description of our holographic imaging approach to improved localization and discrimination of buried underwater UXO. The approach is based on a combination of synthetic aperture sonar (SAS) for spatial localization, and acoustic resonance spectral signatures for target discrimination. The approach is validated using simulated data based on the BOSS platform sensor parameters, and with target models constructed from the exact analytic solution for elastic spheres and spherical shells.

I. INTRODUCTION

This Interim Report describes our results to-date on SERDP project *Advanced SAS Imaging Methods for Resonating Underwater Acoustic Targets* (MR-2322) in support of the Go/No-Go decision.

Buried underwater UXO resides in a challenging region of the acoustic sensing trade space. Downward-looking high frequency ($\gtrsim$ 100 kHz) real aperture sonar systems can provide excellent, high resolution maps of the sediment surface, but attenuate strongly with depth, and fail to provide definitive characterization of buried targets—as quantified, e.g., by high probability of detection ($P_{\rm D}$) and low probability of false alarm ($P_{\rm FA}$). Low frequencies ($\lesssim$ 10 kHz) penetrate the sediment, but provide much poorer spatial resolution—a few "pixels" on a UXO-sized target, but even then, only if a sufficiently large receiver array ($\gtrsim$ 2 m diameter) is available. In terms of the latter, for the purposes of validating our models and approach, during Year 2 of this program we will be generating and analyzing multiple data sets, collected under increasingly realistic conditions, using the buried object scanning sonar (BOSS) system [1].

Motivated, to some extent, by our past work on EMI detection and discrimination of ground-based buried UXO, where metal targets are easy to detect and localize, but much more difficult to identify, our approach is to seek additional spectral signatures in relatively low resolution images of targets that robustly distinguish UXO from similarly sized clutter. Specifically, the holographic technique takes advantage of the fact that hollow metal shells exhibit multiple, distinctive acoustic resonances in precisely the 3–10 kHz band of interest for sediment penetration. Similarly sized solid objects, such as rocks, also exhibit resonances, but generally above 10 kHz. It should be emphasized that resonances of a shell surrounded by sediment (or water) are much less sharp than those of a shell in air ($Q \sim 5$ vs. $\sim 10^2$) due to the much lower acoustic contrast, however our models will show that highly distinctive spectral features still remain, and this is borne out by existing measurements [2, 3].

Since validation, at this point in the program, is primarily based on simulation results, our goal has been to develop a model which is as faithful as possible to the physics, but numerically efficient and easy to work with. We do this by restricting attention to spherical shell targets, for which full exact analytic solutions exist. Although missing some details specific to more elongated UXO geometries, spherical shells nevertheless capture the essential physics of acoustic resonance and target–environment interactions, and provide complete, realistic sonar responses in a computationally efficient manner. They hence form an ideal testing ground for our target imaging and discrimination algorithms. For full validation (in principle, nearly exact) correspondence with experimental data can be made using artificial spherical targets.

We emphasize that, in direct contrast to the ground-based EMI case, in which time domains signatures consist of difficult to interpret, subtly featured power law and multi-exponential decays [4], the target acoustic fingerprint being sought here does not depend on detailed matching to previously collected templates [5]. Rather, we seek only the existence of certain sharp spectral features within the 3–10 kHz bandwidth. As a consequence, our approach lies in an interesting sweet spot, in which the acoustic fingerprint lies in precisely the low frequency band that is both favorable to sediment penetration [6], and provides, through synthetic aperture processing, enough spatial resolution to isolate individual targets.

A. Outline

The outline of the remainder of this document is as follows.

In Sec. II we introduce the acoustic model, including sensor transmitter and receiver characteristics, acoustic dynamics of elastic shells, and how that dynamics is excited by the transmitted wave, and then manifests in the received signals. We show, in particular, that strong resonant features survive the coupling of the shell to the sediment or water environment. Some technical details are relegated to the appendices.

The exact solution for spherical targets exists only when it is embedded in an infinite homogeneous background medium. Approximations are required to treat

a target buried in sediment, which essentially involves ignoring multiple scattering between the target and the sediment surface. These are described in Sec. III.

In Sec. IV we describe the signal processing chain, in which the real-plus-synthetic array data is used to form 2+1D space–frequency images back-projected to a given fixed depth. The spatial image localizes targets at the 10 cm horizontal resolution level. Although detailed target features (e.g., tail fins) are not visible on this scale, the frequency dimension clearly displays the spectral fingerprint. We show as well that, although not directly inferred, the true target depth may be estimated by optimizing over the assumed depth using an image focus metric.

Using the results of the previous sections, in Sec. V we describe simulation studies aimed at validating our approach to UXO localization and discrimination. We describe an automated resonance feature extraction algorithm, and demonstrate its strong false alarm rejection capability.

The reported results strongly support continuation of this program to further validate the holographic method through BOSS system data collects under progressively more realistic field conditions.

II. ACOUSTIC MODEL

The water–sediment–target system includes both fluid and elastic solids components. The water is obviously a fluid, and in the low frequency regime the sediment may be treated as fluid as well [7]. Rocks and metal shells are elastic solids. Depending on its content, the explosive content of the hollow portion of the shell could be either fluid or solid. For simplicity, we will treat it as a fluid, but the results below can easily be generalized if required (the explosive is much less stiff than the metal shell, so its effect on the shell resonances is, in any case, relatively small). A reasonable fidelity physics-based model of this system must include the interacting dynamics of all of these components.

A. Elastodynamic equations

The linearized dynamics of a homogeneous elastic medium (with fluids included as a special case) is governed by the equation [8]

$$\rho \partial_t \mathbf{v} = \nabla \cdot \hat{\boldsymbol{\tau}}, \tag{2.1}$$

in which ρ is the (static) background mass density, $\mathbf{v}$ is the velocity field and $\hat{\boldsymbol{\tau}}$ is the elastic stress tensor. For an isotropic medium, the latter takes the form

$$\hat{\boldsymbol{\tau}} = \lambda \nabla \cdot \mathbf{s} \mathbb{1} + \mu \left[\nabla \mathbf{s} + (\nabla \mathbf{s})^T \right], \tag{2.2}$$

where λ, μ are elastic constants, and $\mathbf{s}$ is the displacement field, which sends the volume element at $\mathbf{x}$ to $\mathbf{x} + \mathbf{s}(\mathbf{x})$, and in terms of which $\mathbf{v} = \partial_t \mathbf{s}$. We neglect frictional dissipation here and in all that follows. This may be modeled as well (via addition of viscous terms to $\boldsymbol{\tau}$), but at the lower frequencies of interest here, this is a lower order effect. In component form one has $\hat{\tau}_{\alpha\beta} = \lambda(\nabla \cdot \mathbf{s})\delta_{\alpha\beta} + \mu \left[\partial_\alpha s_\beta + \partial_\beta s_\alpha \right]$. The shear elastic constant μ distinguishes solids and fluids, and vanishes for the latter.

Substituting (2.2) into (2.1), one obtains the explicit form

$$\rho \partial_t^2 \mathbf{s} = (\lambda + \mu) \nabla (\nabla \cdot \mathbf{s}) + \mu \nabla^2 \mathbf{s}. \tag{2.3}$$

If $\mathbf{s} = \mathbf{s}_T$ is transverse, $\nabla \cdot \mathbf{s}_T = 0$, then (2.3) reduces to the wave equation

$$\partial_t^2 \mathbf{s}_T = c_T^2 \nabla^2 \mathbf{s}_T, \quad c_T = \sqrt{\frac{\mu}{\rho}}. \tag{2.4}$$

with transverse (shear) sound speed c_T. There are two independent transverse polarizations (i.e., displacement orthogonal to the wavevector). Similarly, if $\mathbf{s} = \mathbf{s}_L$ is longitudinal, $\nabla \times \mathbf{s}_L = 0$, one finds $\nabla(\nabla \cdot \mathbf{s}_L) = \nabla^2 \mathbf{s}_L$, and hence

$$\partial_t^2 \mathbf{s}_L = c_L^2 \nabla^2 \mathbf{s}_L, \quad c_L = \sqrt{\frac{\lambda + 2\mu}{\rho}}, \tag{2.5}$$

with longitudinal (compressional) sound speed c_L. There is only a single longitudinal polarization (displacement collinear with wavevector).

For $\mu = 0$, c_T vanishes as well, and only the usual longitudinal sound waves survive. Shear flow, for which there is no elastic restoring force, may still exist but will be neglected here—we will consider only acoustic excitations of an otherwise (nearly) stationary fluid.

B. Boundary conditions

Equations (2.1)–(2.5) are valid in the interior of a homogeneous region. In order to describe the dynamics of more complex media, composed of two or more different homogeneous media, one must impose boundary conditions at their interfaces. These are: (i) continuity of $\mathbf{s}$ (the medium does not tear or cavitate), and (ii) continuity of the traction $\hat{\mathbf{n}} \cdot \hat{\boldsymbol{\tau}}$ (consistency of the local body forces across the boundary), in which $\hat{\mathbf{n}}$ is the local surface normal.

For a boundary between elastic media, each of these yields three conditions, for a total of six, consistent with the three possible polarizations in each region. For a fluid-elastic boundary, (i) is replaced by continuity only of the normal displacement, $\mathbf{s} \cdot \hat{\mathbf{n}}$ (free slip boundary condition). This a total of four conditions, consistent with the absence of the two transverse polarizations in the fluid.

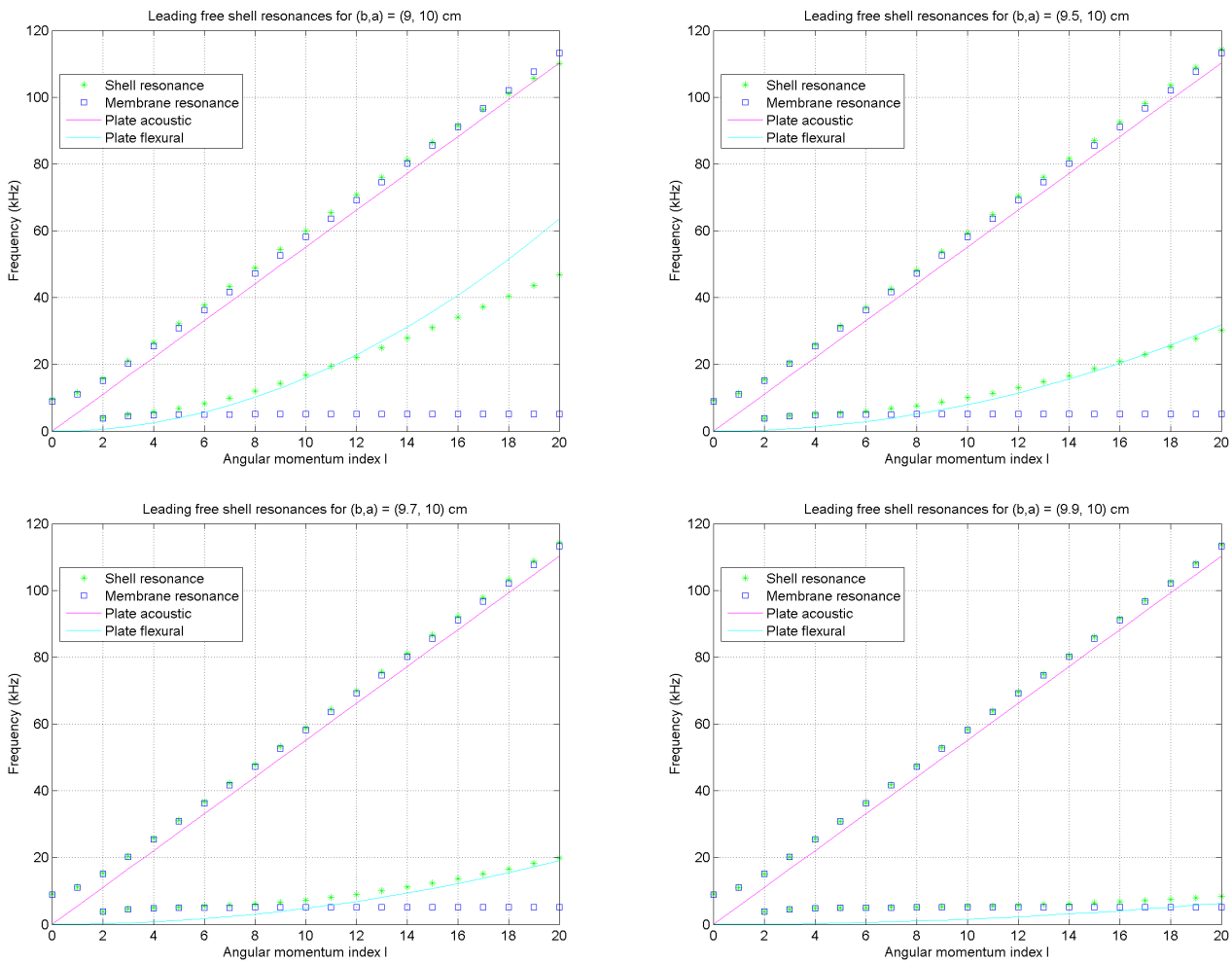

FIG. 1: Lowest order resonant frequencies for a thin spherical shell (with $b/a = 0.9, 0.95, 0.97, 0.99$), computed from the vanishing of the determinant of the 4×4 block $\mathcal{M}(a, b)$ described below (B13). The membrane curves ($\delta = a - b \to 0$; the same in all plots) are computed from the vanishing of the determinant of (B22) ($l > 0$) or (B23) ($l = 0$). For $l \geq 2$ there are two branches, with the lower one corresponding to (volume preserving) flexural waves and the upper one to (acoustic) stretching waves. For $l = 0, 1$ the flexural mode is absent. The acoustic mode is well approximated by corresponding 2D plate dispersion (B26), which is independent of thickness. Consistent with (B28), with increasing l the shell flexural mode crosses over from the essentially frequency independent membrane flexural mode to the quadratic flat plate dispersion (B27). For $b/a = 0.9$, hence $a/\delta = 10$, one indeed sees deviations from the flat plate form for $l \gtrsim 10$ as the wavelength becomes smaller than the shell thickness.

C. Exact solutions for spherical geometries

Exact solutions to the elastodynamic equation (2.3) are few and far between, even more so due to the vector nature of the displacement field $\mathbf{s}$. Numerical implementation, even for relatively simple nontrivial target shapes, is also challenging, given especially that the target interacts strongly with its environment and a full description of the measurement encompasses a broad range of spatial scales, much larger than the target volume.

General concentric spherical shell structures are the only compact targets for which exact solutions can be constructed. Due to the high symmetry, the detailed resonant response spectrum of a spherical shell will never accurately approximate that of an elongated shell. However, the complexity of the dependence of the coupling to the environment, interaction with an incident wave, etc., is fully captured. This allows one to explore the key UXO detection and discrimination questions that lie at the heart of the present effort. Higher fidelity modeling of more realistic targets, e.g., to achieve greater insight into the variability of the spectral signature, is of future interest, but is not required to answer the more basic questions pursued here.

In App. A we describe the Bessel–spherical harmonic basis functions appropriate to spherical geometries, and in App. B we use these to exhibit the detailed solution for a hollow elastic spherical shell, with a fluid filled spherical

void and a lying in an unbounded fluid background [9]. In App. C the results are used to compute the scattered field generated by a known transmitted wave.

D. Free vibrational modes

In the limit in which the two fluids are treated as vacuum, the spherical shell has undamped modes of free vibration. Some key features of these modes are shown in Fig. 1, where results for a shell with outer radius $a = 10$ cm, and four different inner radii ($b = 9, 9.5, 9.7, 9.9$ cm), are shown and compared to results for a spherical membrane (thickness $\delta = a - b \to 0$), and for an infinite 2D plate with the same thickness (see App. B 2 c). In all cases, the same parameters ρ, λ, μ are used, derived from assumed bulk sound speed values $c_T = 2$ km/s, $c_L = 4$ km/s, and mass density $\rho = 4$ g/cm^3. In the plots one should think of the spherical harmonic index as roughly the number of wavelengths fitting within a perimeter, so that $\lambda_l \sim 2\pi a/l$.

The first feature to note is that there are two branches: (a) a higher dilatation branch $f_l^{\rm d}$ characterized mainly by patterns of stretching and contraction of the shell; and (b) a lower flexural branch $f_l^{\rm fl}$ (beginning at $l = 2$, for geometric reasons), corresponding to local bending, with little stretching—essentially "ripples" on the shell. The latter branch becomes almost completely flat, independent of l, consistent with vanishing bending energy, in the membrane limit (why the mode frequencies do not then vanish identically is explained below).

The second feature to note is how weakly the lower frequency modes depend on shell thickness. The lowest frequency modes, which are the focus of the present work, are nearly independent of the thickness (though not of the radius, scaling rather as c_L/a). The lowest flexural mode frequency, $f_2^{\rm fl} \simeq 4$ kHz, is less than half that of the lowest acoustic mode, $f_0^{\rm d} \simeq 10$ kHz. Moreover, even for $\delta = 1$ cm (which is in the range expected for UXO), there are several flexural modes, out to about $l = 6$, that still lie below 10 kHz, precisely within the range of interest.

The trend of these modes with δ and l may be understood by comparing them to those corresponding to an infinite flat plate of the same thickness [8] (solid magenta and cyan lines in the figure). Both of these approach zero frequency at small wavenumber $k = 2\pi/\lambda \sim l/a$ (the dilatation branch linearly as $c_0 k$, with $c_0 = 2c_T\sqrt{1-(c_T/c_L)^2}$, the flexural branch quadratically as $D_0 k^2$, with $D_0 = c_0\delta/2\sqrt{3}$). The finite frequency for the sphere reflects both the lower bound on the wavenumber, $ka \gtrsim 1$, and the finite bending modulus of even an infinitely thin curved surface (due to "crinkling" effects that forbid bending without some stretching). It is the k^2 scaling that also explains the flatness of the flexural branch at low frequency, and hence the weak dependence of the first few mode frequencies on l. This becomes increasingly more pronounced as $\delta \to 0$.

The above features are to be contrasted with the results, shown in Fig. 2, for a solid sphere with the same radius $a = 10$ cm, mimicking, say, a rock. The flexural mode analogues are now pushed to much higher frequencies, have linear rather than quadratic dispersion, and all modes lie above 8 kHz.

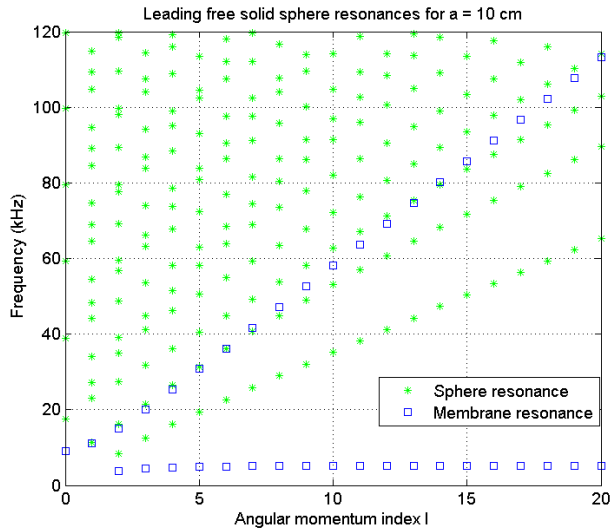

FIG. 2: Resonant frequencies for a solid sphere with radius $a = 10$ cm. The membrane spectrum, identical to that in Fig. 1, is still displayed for comparison. The multiplicity of modes for each l is due to nonzero values of the radial wavenumber, which are of much higher frequency for thin shells (radial wavelength requirement $\lambda_r \lesssim \delta$ yields frequencies $f \gtrsim c_T/\delta, c_L/\delta$). The flexural and dilatational mode analogues correspond, respectively, to the lowest and second lowest line of green stars.

Given the basic geometric origin of the shell mode branches (dilatation and bending of a smooth, curved surface), we expect the basic low frequency mode features to survive to more realistic UXO shapes. Thus, even though the breaking the spherical symmetry will split the two branches into several sub-branches (the modes in both Figs. 1 and 2 have the usual $2l + 1$ degeneracy), we still expect (i) the lowest dilatation mode frequency to scale as c_0/a, (ii) the lowest flexural mode frequency to lie a factor of two or so lower, and (iii) several flexural mode frequencies to lie near the lowest one, due to the flatness of the band. These are key signatures that will help distinguish hollow from solid targets. We emphasize that UXO-sized targets should be resolved in the holographic images, to be described below, so that an *a priori* size estimate will be available. This will help remove uncertainty based on comparing frequency spectra for widely differing target sizes (e.g., a much larger rock could have mode frequencies in the 4 kHz range).

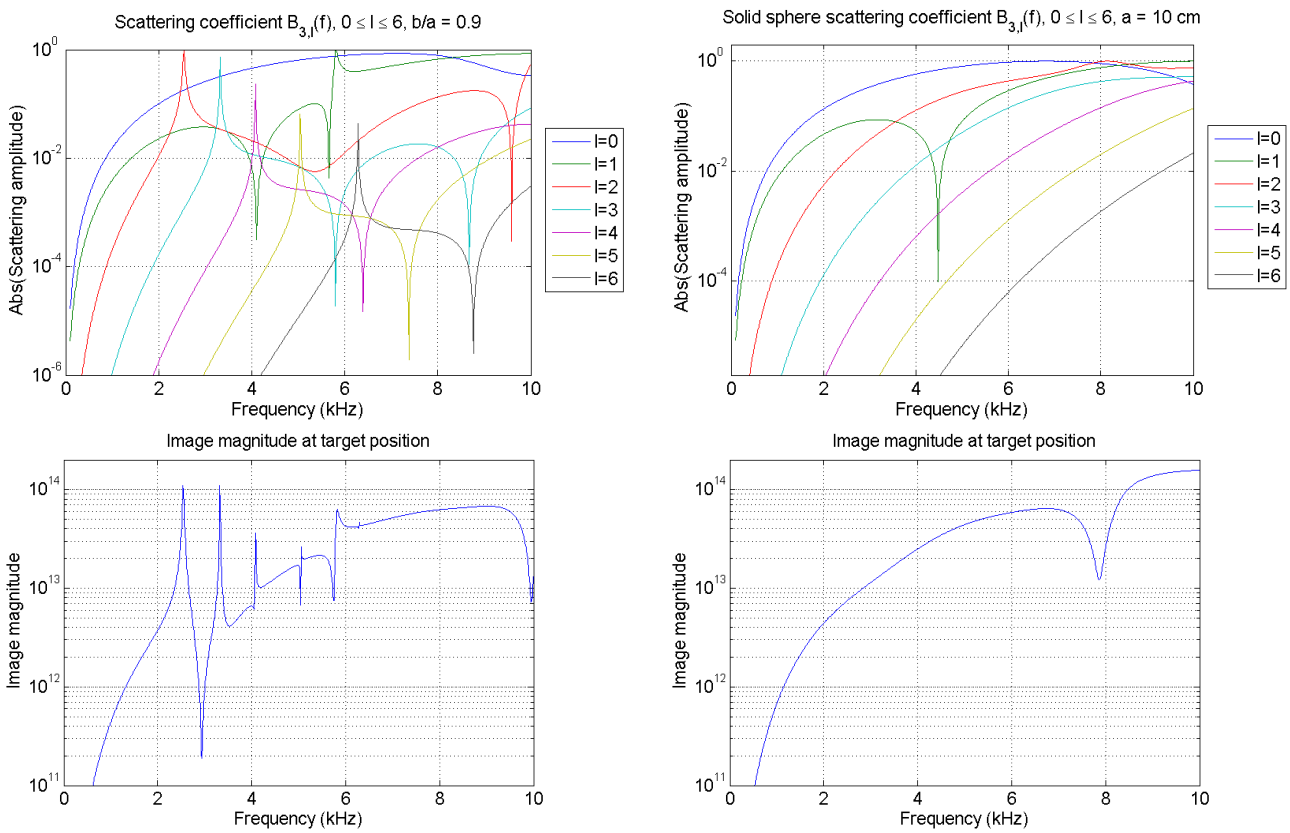

FIG. 3: **Top row:** Scattered wave amplitude spectra $B_{3,l}(f)$ for each angular momentum index in the range $0 \leq l \leq 6$ (normalized to a unit incident wave amplitude, $A_{3,l} = 1$; see App. B for definitions of the parameters). **Left:** Target is a shell (with the same material parameters as in Fig. 1) with outer and inner radii $a = 10$ cm, $b = 9$ cm, and both the hollow and background fluids are taken to be water (mass density $\rho = 1$ g/cm^3, sound speed $c = 1500$ m/s). The remnants of the low frequency free resonances still appear as sharp peaks (the downward pointing cusps are not singularities, but unresolved zero-crossings on the log scale). The visible dilatation modes ($l = 0, 1$) are strongly broadened, but the flexural modes are quite sharp (they radiate much less efficiently), and the first few ($l = 2, 3, 4$) lie below 5 kHz. The nominal resonant frequencies are lower than those in the upper left panel of Fig. 1 due to the extra inertial mass provided by the coupled motion of the surrounding fluid. **Right:** Target is now a radius $a = 10$ cm solid sphere. All resonant features below 10 kHz have disappeared (the downward-pointing cusp is again an unresolved zero crossing). **Bottom row:** Total spectral response obtained from the frequency dependence of the holographic imaging equation (4.1) at the target pixel using the BOSS parameters, with target centered 3 m below the synthetic grid (the same parameters used to generate Fig. 4). The targets match those in the top row. The dip near 8 kHz on the right is clearly a reflection of the $l = 1$ zero crossing on the left, but shifted in frequency due to the added background provided by the other modes. One should therefore view it as a mode superposition interference effect, not as a resonance feature.

E. Homogeneous background medium effects

Targets are not sensed in isolation, but embedded in a dense (fluid and/or sediment) background medium. The acoustic coupling to the environment enables but also dampens the free oscillations by through radiation of acoustic energy, broadening the resonant features. The results shown in Fig. 3 demonstrate, however, that the acoustic scattering response still exhibits sharp peaks in the low frequency regime of interest. The top row shows the normalized responses for a sequence of individual l values. The bottom row shows the resulting holographic image spectral response (Sec. IV) at the target pixel, which contains a linear superposition of the individual modes. The key feature is that first two peaks are very strong, and would be expected to contribute to a robust target fingerprint. The remaining peaks are of significantly lower magnitude (note the logarithmic scale), and might not stand out as well under realistic clutter conditions.

III. BURIED TARGET MODELS

We next consider generalization of the model to the case of a buried target. Analytic results are no longer available, even for spherical scatterers, so we limit ourselves to approximate models which should still capture

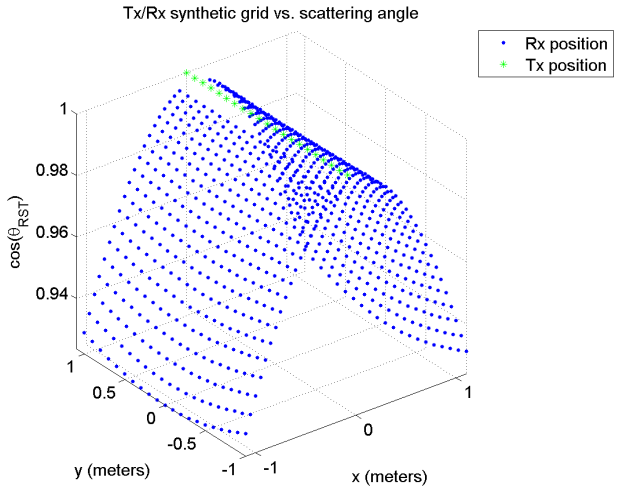

FIG. 4: The transmitter-receiver grid, using BOSS parameters, corresponding to the synthetic aperture that is used to construct the holographic image, plotted vs. transmitter-target-receiver scattering angle $\theta_{\rm RST}$ for a target centered at $x = y = 0$, 3 m below the receiver plane. The green stars correspond to the sequence of 10 cm spaced transmitter positions along the platform line of motion, taken as the y-axis. Each set of 40 blue stars sharing the same y-coordinate correspond to the receiver positions along the two BOSS wings. A received scattered signal is measured (only) for each of the 40 Tx-Rx pairs sharing the same platform position. As discussed in the text, the variation in $\cos(\theta_{\rm RST})$ across the grid quantifies the possible influence of bistatic scattering effects that are neglected in the imaging equation.

the essential phenomenology. The two effects of main interest are (a) changes in the effective path lengths from transmitter to scatterer, and back to receiver, and (b) background contributions to the signal from the direct scattering from the sediment surface. The effects (c) of reverberation (multiple scattering) between the target and the sediment surface, which are what forbids an exact solution, are neglected.

We treat the sediment as a fluid, defined by sound speed $c_{\rm sed} \simeq 1700$ m/s, and density $\rho_{\rm sed} \simeq 1.9$ g/cm^3. In a more general treatment, porous medium dynamics results in a frequency-dependent sound speed $c_{\rm sed}(\omega)$ [14–16].

We will ignore the effects of back-reflections from the sediment boundary on the intrinsic dynamics of the elastic target [12]. Thus, we will assume that the local Bessel-spherical harmonic expansion (B2) of the transmitted wave (see below) continues to determine the local outgoing wave expansion (C5). The sediment is therefore treated, for this aspect of the calculation, as homogeneous and infinite.

To summarize, the measured signal estimation is comprised of the following key steps (see Fig. 5): (1) A ray tracing (geometrical optics) approach, including appropriate transmission and reflection coefficients at the sediment surface, will be used to estimate the transmitted field, in the form of a local plane wave, in the neighborhood of the buried scatterer. (2) The expansion of this plane wave, according to (B3) and (C2), then leads to a local scattered wave expansion of the form (C5). (3) A ray tracing approach is again used to propagate this local scattered wave back to the receiver, including the reverse transmission coefficient through the sediment surface. (4) The direct reflection of the transmitted wave from the sediment will generate a background signal. The backprojection image (4.1) should attenuate the dominant direct reflection, but for a rough surface there will be non-specular returns (with similar transit times) that will be enhanced. The latter should ultimately be included as part of the clutter model.

A. Transmitted wave in target neighborhood

We continue to model the transmitted wave, prior to interaction with the sediment, as an outgoing spherical wave

$$\mathbf{s}_T = \frac{A_0}{ik}\nabla\frac{e^{ik|\mathbf{x}-\mathbf{x}_T|}}{4\pi|\mathbf{x}-\mathbf{x}_T|}, \tag{3.1}$$

in which the amplitude A_0 (with dimensions of area) is determined by the physical properties of the transmitter. In the vicinity of the target center $\mathbf{x}_S$ one may then approximate

$$\mathbf{s}_T = A_0\mathcal{T}(\mathbf{x}_T,\mathbf{x}_S)\hat{\mathbf{k}}^T e^{i\mathbf{k}^T\cdot(\mathbf{x}-\mathbf{x}_S)} \tag{3.2}$$

in which the transmission coefficient is given by

$$\mathcal{T}(\mathbf{x}_T,\mathbf{x}_S) = T_0 e^{i(k|\mathbf{x}_T-\mathbf{x}_I|+k^T|\mathbf{x}_S-\mathbf{x}_I|)} \tag{3.3}$$

where T_0 is an amplitude [see (3.10)] and $\mathbf{x}_I$ is the point where the ray intersects the sediment surface. The latter is derived from Fermat's principle, which minimizes the propagation time $t = |\mathbf{x}_T-\mathbf{x}_I|/c_w + |\mathbf{x}_T-\mathbf{x}_I|/c_{\rm sed}$. The result is Snell's law of refraction,

$$\frac{\sin(\theta_w)}{\sin(\theta_{\rm sed})} = \frac{c_w}{c_{\rm sed}}, \tag{3.4}$$

in which $\theta_w, \theta_{\rm sed}$ are, respectively, the incident and refracted ray angles relative to the sediment surface normal (see Fig. 5). This result can be converted into a quartic equation for the unknown horizontal position of $\mathbf{x}_I$:

$$\left[1-\frac{c_w^2}{c_{\rm sed}^2}\right]x^2(L-x)^2+h_S^2x^2-\frac{c_w^2}{c_{\rm sed}^2}h_T^2(L-x)^2 = 0. \tag{3.5}$$

Here $h_S = z_{\rm sed} - z_S$ is the target center depth, $h_T = z_T - z_{\rm sed}$ the transmitter height (both relative to the sediment surface $z_{\rm sed}$), L the horizontal distance between transmitter and target, and x is the unknown horizontal distance of $\mathbf{x}_I$ from $\mathbf{x}_T$. One has the relationships

$$\sin(\theta_w) = \frac{x}{\sqrt{x^2+h_w^2}},\ \sin(\theta_{\rm sed}) = \frac{L-x}{\sqrt{(L-x)^2+h_S^2}}. \tag{3.6}$$

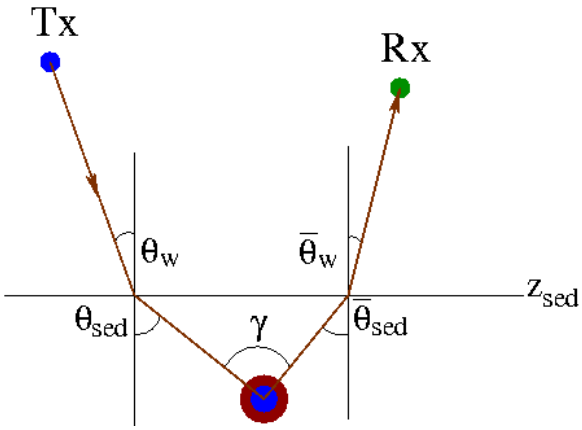

FIG. 5: Ray tracing geometry underlying the received signal calculation. The incident ray (left) is refracted at the sediment surface, and scatters from the target. The return ray (right) is again refracted before arriving at the receiver. The refraction angles obey Snell's law (3.4), and the scattering angle enters (3.13).

An identical calculation (see below) determines the ray path of the scattered wave, from $\mathbf{x}_S$ back to the receiver $\mathbf{x}_R$.

The reflection and transmission coefficients are obtained from continuity of the normal components of the displacement and the traction. In the neighborhood of the point $\mathbf{x}_I$ one has a local plane wave expansion

$$\begin{aligned} \mathbf{s}_T &\approx A_0 \frac{e^{ik|\mathbf{x}_I-\mathbf{x}_T|}}{4\pi|\mathbf{x}_I-\mathbf{x}_T|} \\ &\times \begin{cases} \hat{\mathbf{k}} e^{i\mathbf{k}\cdot(\mathbf{x}-\mathbf{x}_I)} + R_I \hat{\mathbf{k}}^R e^{i\mathbf{k}^R\cdot(\mathbf{x}-\mathbf{x}_I)}, & z > z_{\rm sed} \\ T_I \hat{\mathbf{k}}^T e^{i\mathbf{k}^T\cdot(\mathbf{x}-\mathbf{x}_I)}, & z < z_{\rm sed}, \end{cases} \end{aligned} \tag{3.7}$$

in which $\mathbf{k}$ is parallel to $\mathbf{x}_I - \mathbf{x}_T$ and $\mathbf{k}^T$ is parallel to $\mathbf{x}_S - \mathbf{x}_I$. Thus, one may write $\mathbf{k} = (\mathbf{k}_\perp, k_z)$, $\mathbf{k}^R = (\mathbf{k}_\perp, -k_z)$, $\mathbf{k}^T = (\mathbf{k}_\perp, k_z^T)$, $k_z = \sqrt{(\omega/c_w)^2 - k_\perp^2}$, $k_z^T = \sqrt{(\omega/c_{\rm sed})^2 - k_\perp^2}$, and $k_\perp/k = \sin(\theta_w)$, $k_\perp/k^T = \sin(\theta_{\rm sed})$. Defining the combination

$$Z = \frac{\cos(\theta)}{\rho c}, \tag{3.8}$$

one obtains

$$\begin{aligned} R_I &= \frac{Z_w - Z_{\rm sed}}{Z_w + Z_{\rm sed}} \\ T_I &= \frac{\rho_w c_w}{\rho_{\rm sed} c_{\rm sed}} \frac{2Z_w}{Z_w + Z_{\rm sed}}. \end{aligned} \tag{3.9}$$

In terms of these quantities, one obtains for the coefficient T_0 in (3.2):

$$T_0 = \frac{T_I}{4\pi|\mathbf{x}_T - \mathbf{x}_S|}, \tag{3.10}$$

in which the geometric spreading factor in the denominator is only approximate, but is adequate for shallow targets, not too off-normal incidence, and $c_w/c_{\rm sed}$ not too different from unity. Refraction of the ray is a nonlinear, anisotropic process, and in general entails a much more complicated dependence of (3.10) on $\mathbf{x}_S - \mathbf{x}_I$ [17].

B. Scattered wave

The scattered wave in the neighborhood of the target, prior to its interaction with the sediment surface, takes a form similar to (C5):

$$\mathbf{s}_{\rm sc}(\mathbf{x}) = \sum_{l,m} A_{lm}(k^T) B_{3,l}(k^T) \mathbf{s}_{L,lm}[h_l^{(1)}(k^T|\mathbf{x}-\mathbf{x}_S|)], \tag{3.11}$$

in which the scattered wave amplitudes $B_{3,l}(k^T)$ are computed from (B11)–(B13) using the sediment parameters for the background medium. The incident wave amplitudes are given by

$$A_{lm}(k^T) = 4\pi A_0 (-i)^{l+1} \mathcal{T}(\mathbf{x}_T, \mathbf{x}_S) Y_{lm}^*(\theta^T, \phi^T), \tag{3.12}$$

in which θ^T, ϕ^T are the polar angles associated with the direction $-\mathbf{k}^T$ (parallel to $\mathbf{x}_I - \mathbf{x}_S$), and $\mathcal{T}$ is given by (3.3), (3.9) and (3.10).

The pressure signal, generalizing (C6), takes the form:

$$\begin{aligned} p_{\rm sc}(\mathbf{x}) &= A_0 \rho_{\rm sed} c_{\rm sed}^2 k^T \mathcal{T}(\mathbf{x}_T, \mathbf{x}_S) \sum_l (2l+1)(-i)^{l+1} \\ &\times B_{3,l}(k^T) h_l^{(1)}(k^T|\mathbf{x}-\mathbf{x}_S|) P_l[\cos(\gamma)], \end{aligned} \tag{3.13}$$

in which γ is the angle between $-\mathbf{k}^T$ (hence, $\mathbf{x}_I - \mathbf{x}_S$) and $\mathbf{x} - \mathbf{x}_S$.

C. Received wave

Using $h_l(x) \approx (-i)^{l+1} e^{ix}/x$, valid for large x, and tracing the outgoing wave back to the receiver, one obtains

$$\begin{aligned} p_{\rm sc}(\mathbf{x}_R) &\approx 4\pi A_0 \rho_w c_w c_{\rm sed} \mathcal{T}(\mathbf{x}_T, \mathbf{x}_S) \bar{\mathcal{T}}(\mathbf{x}_S, \mathbf{x}_R) \\ &\times \sum_l (-1)^{l+1} (2l+1) B_{3,l}(k^T) P_l[\cos(\gamma)], \end{aligned} \tag{3.14}$$

in which

$$\bar{\mathcal{T}}(\mathbf{x}_S, \mathbf{x}_R) = \bar{T}_0 e^{i(k^T|\bar{\mathbf{x}}_I - \mathbf{x}_S| + k|\mathbf{x}_R - \bar{\mathbf{x}}_I|)} \tag{3.15}$$

with return intersection point $\bar{\mathbf{x}}_I$, amplitude [compare (3.10)]

$$\bar{T}_0 = \frac{\bar{T}_I}{4\pi|\mathbf{x}_R - \mathbf{x}_S|} \tag{3.16}$$

and coefficients [compare (3.9)]

$$\begin{aligned} \bar{R}_I &= \frac{\bar{Z}_{\rm sed} - \bar{Z}_w}{\bar{Z}_w + \bar{Z}_{\rm sed}} \\ \bar{T}_I &= \frac{\rho_{\rm sed} c_{\rm sed}}{\rho_w c_w} \frac{2\bar{Z}_{\rm sed}}{\bar{Z}_w + \bar{Z}_{\rm sed}}. \end{aligned} \tag{3.17}$$

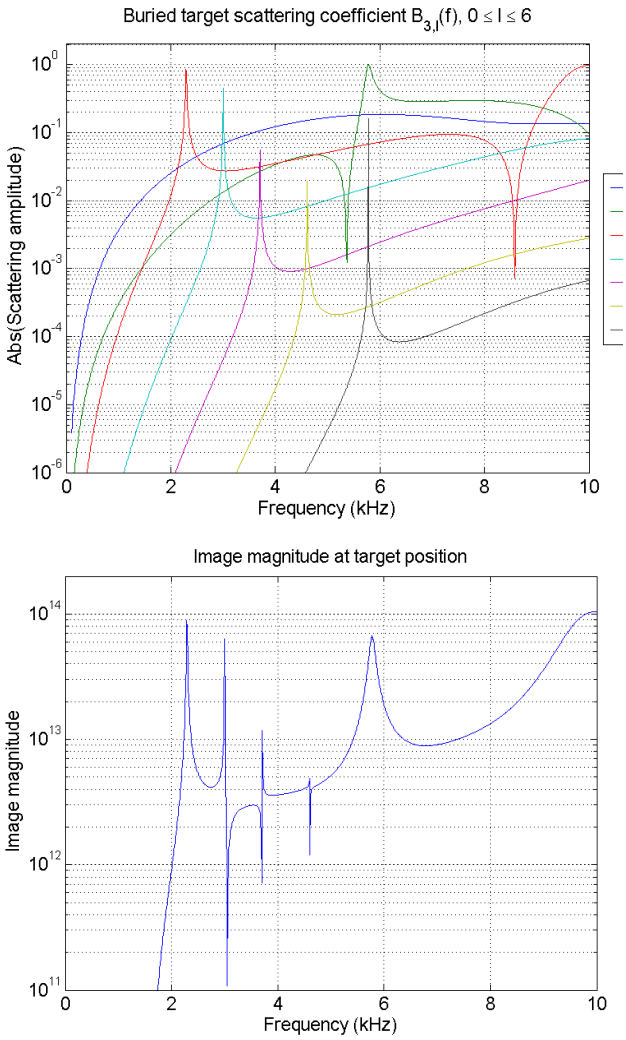

FIG. 6: Scattering amplitudes $B_{3,l}(f)$ for a buried spherical shell, with parameters the same as those used in the left column of Fig. 3. As described in Sec. III, these are computed as if the sediment were infinite and homogeneous, and then inserted into (3.13) to propagate them through the sediment surface and compute the received signal. The sediment properties are $c_{\rm sed} = 1700$ m/s, $\rho_{\rm sed} = 1.9$ g/cm^3. The hollow portion is still treated as water. The resonant features remain sharp, though they are shifted in frequency due to the changed background.

The bars indicate that the diffraction angles $\bar{\theta}_w, \bar{\theta}_{\rm sed}$ refer to the return path (see Fig. 5), calculated according to (3.5), but with L now referring to the horizontal separation of $\mathbf{x}_S$ and $\mathbf{x}_R$, and x to the horizontal distance between $\mathbf{x}_S$ and $\bar{\mathbf{x}}_I$. The angle γ is between the directions $\bar{\mathbf{x}}_I - \mathbf{x}_S$ and $\mathbf{x}_I - \mathbf{x}_S$ (see Fig. 5).

Equation (3.14) is derived from (3.11) by expanding the gradient of the Hankel function in a local longitudinal plane wave in the neighborhood of $\bar{\mathbf{x}}_I$ [analogous to (3.7)], and neglecting the gradient of the spherical harmonic factor (consistent with the large argument approximation). It may also be derived directly from (3.13) if

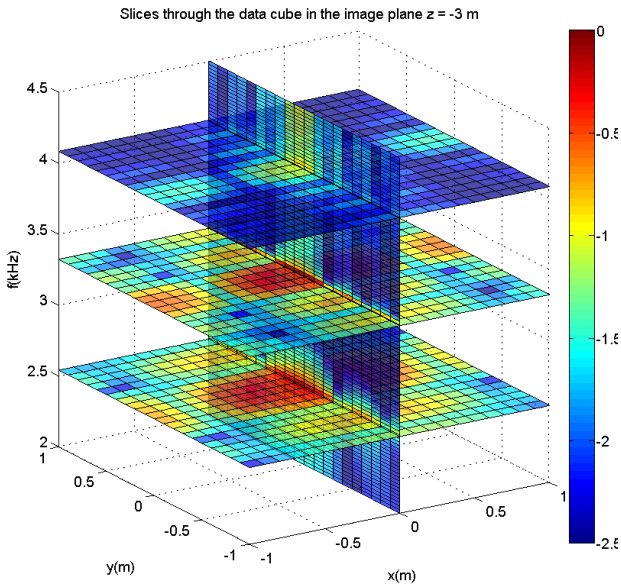

FIG. 7: Slices through the space-frequency holographic image cube generated by (4.1) and (4.2) for a target in the water column. The target lies at the horizontal origin, $x = y = 0$, and the image is backprojected to the plane $z = -3$ m, coinciding with the target depth. The fixed frequency slices are at the first three peaks ($f = 2.54, 3.32, 4.08$ kHz) in the lower left plot in Fig. 3. As in that figure, the colorbar represents a logarithmic scale.

one notes that the pressure wave transmission coefficient is obtained by dropping the $\rho_{\rm sed} c_{\rm sed}/\rho_w c_w$ prefactor in $\bar{T}_I$. The denominator in (3.16) is again approximate—see the comments below (3.10).

D. Nonspecular surface reflection

Note that the reflection coefficient R_I in (3.9) defines the received ground bounce, but at a different sediment surface point defined by direct reflection back to the receiver. For a rough surface, reflection is also nonspecular, and this will lead to background clutter contributions that will be incorporated in a later iterations of the model.

IV. HOLOGRAPHIC IMAGE FORMATION

We now describe the methodology for creating 2+1D space-frequency images that lie at the heart of our UXO detection and discrimination approach. We will first consider the simpler case of targets in the water column, and then generalize to buried targets.

A. Proud target imaging equation

The expression (C6) derived in App. C for the scattered acoustic pressure field $p_{\rm sc}(\mathbf{r})$ determines the received signal for a target in a homogeneous background medium. In a scattering measurement, the variables r, θ, ϕ in (C6) correspond to the polar coordinates of the receiver position $\mathbf{x}_R$ relative to the sphere center. In an imaging modality, measurements are taken for a large set of transmitter-receiver pairs $\{\mathbf{x}_{T,n}, \mathbf{x}_{R,n}\}_{n=1}^N$ over a band of frequencies $\omega = 2\pi f$. The BOSS platform measurement grid is described in Fig. 4. The objective is to use these results to characterize and spatially localize the scatterer. Note that the intrinsic target resonance features are contained in the scattered wave amplitudes $B_{3,l}(k)$, and should therefore produce sharp features as function of frequency $\omega = ck$ in the measured signals.

The actual measured signals $\phi_n(\omega) = p_{\rm sc}(\mathbf{x}_R; \mathbf{x}_T, \omega)$ are assumed to be directly related to the local pressure field. However, this relationship is often achieved only after substantial calibration of the raw voltage signals. The latter depend on the spatial distribution of pressure $p_{\rm sc}(\mathbf{r})$ over the physical receiver elements. The resulting receiver sensitivity pattern will, in general, depend on both frequency and the direction of arrival (e.g., via the relative direction between the receiver element surface normal $\hat{\mathbf{n}}$ and the pressure gradient, $\hat{\mathbf{n}} \cdot \nabla p_{\rm sc}$). This dependence must be carefully calibrated in advance in order to for the resulting data products to be quantitatively meaningful.

Specializing to the point transmitter model (C3), the holographic (fixed frequency) backprojection takes the form:

$$\mathcal{I}(\mathbf{x}, \omega) = \sum_{n=1}^{N} \phi_n(\omega) \mathcal{A}_n(\mathbf{x}) e^{-ik\rho_n(\mathbf{x})}, \tag{4.1}$$

in which

$$\rho_n(\mathbf{x}) = |\mathbf{x}_{T,n} - \mathbf{x}| + |\mathbf{x}_{R,n} - \mathbf{x}| \tag{4.2}$$

is the two-way distance from transmitter to the nominal scatterer position $\mathbf{x}$, and the amplitude

$$\mathcal{A}_n(\mathbf{x}) = (4\pi)^2 |\mathbf{x}_{T,n} - \mathbf{x}||\mathbf{x}_{R,n} - \mathbf{x}| \tag{4.3}$$

compensates for the two-way geometrical spreading. In the far field limit (large Bessel function arguments) the product

$$A_l(k) h_l^{(1)}(kx_R) \approx 4\pi A_0 (-i)^{l+1} \frac{e^{ik(x_T + x_R)}}{x_T x_R} \tag{4.4}$$

is seen to cancel the factor (4.1) when $\mathbf{x} = 0$, coinciding with the sphere center. This should lead to a strong peak in $\mathcal{I}(\mathbf{x}, \omega)$ near the origin, and, in addition, a strong spectral variability of that peak through the amplitudes $B_{3,l}(k)$.

Note that for $l > 0$ the angular dependence of the Legendre polynomials in (C6) enters and will quantitatively modify the result. However, since $P_l(1) \equiv 1$, the modification will only be substantial if the transmitter-receiver separation $|\mathbf{x}_T - \mathbf{x}_R|$ becomes a significant fraction of the standoff distance, i.e., for close-in, wide-angle (T-matrix style) measurements [12, 13]. To quantify this, the vertical axis in Fig. 4 shows the variation in $\cos(\theta_{\rm RST})$ across the array for a target centered 3 m below the measurement grid, where $\theta_{\rm RST}$ is the angle between the transmitted and received rays. The fact that it so close to unity indicates that bistatic effects should be negligible.

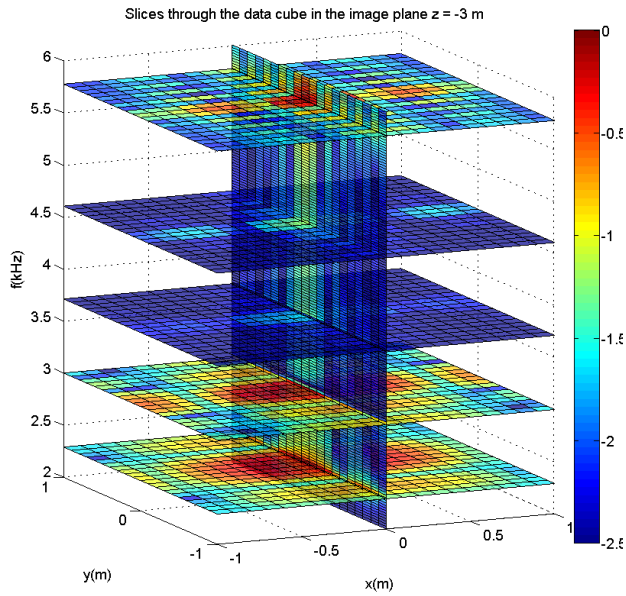

FIG. 8: Slices through the space-frequency holographic image cube generated by (4.1) using the acoustic path length (4.5) appropriate to a buried target. The target lies at the horizontal origin, $x = y = 0$, and the image is backprojected to the plane $z = -3$ m, coinciding with the target depth, with sediment surface at $z = -2.5$ m. The fixed frequency slices are at the first five peaks ($f = 2.29, 3.0, 3.71, 4.60, 5.77$ kHz) in the lower plot in Fig. 6. The color bar again represents a logarithmic scale.

In Fig. 7 we show slices through the image cube generated by the same model as in the left column of Fig. 3, backprojected to the true 3 m target depth. Spatial localization of the target, lying at the horizontal origin, is consistent with the predicted ∼20 cm resolution based on the wavelength c/f (which then improves with increasing frequency). The "hot spots" due to the first two resonant features are evident. The third resonant feature is visible as well, but much less distinctive. Images for solid targets show no such features.

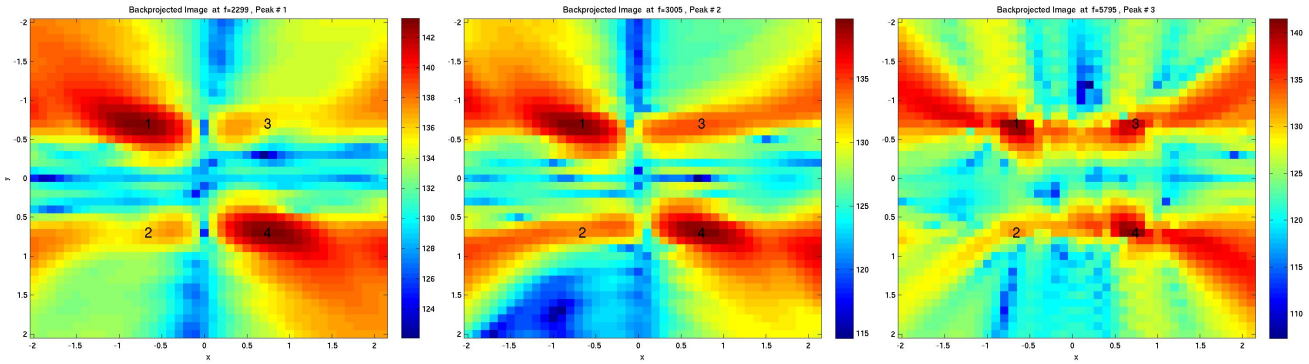

FIG. 9: Fixed frequency slices of the holographic image cube ($f = 2299, 3005, 5796$ Hz, left to right, corresponding to the three strongest peaks in the measured response of 10 cm hollow shell—bottom panel of Fig. 6). The images are created using four buried targets, placed on the corners, $(x, y) = (\pm 0.5, \pm 0.5)$ m, of a centered 1 m square, all at 0.5 m depth, 3 m below the receiver grid. The data is backprojected to this same $z = -3$ m image plane. Targets 1, 4 are the same 10 cm radius shells used in Fig. 6; target 2 is a 5 cm radius solid "rock"; target 3 is a 10 cm radius solid "rock". The targets are clearly resolved, though some outwards "bleeding" of amplitude in the x-coordinate is observed due to the limited 2 m physical aperture (BOSS wingspan) in this direction. In a "video" scan through frequency (not shown), the two shells "flash" at the frequencies exhibited here, while the rocks exhibit a smoothly varying frequency response.

B. Buried target imaging equation

The generalization of (4.1) to buried targets replaces (4.2) by the total acoustic path length

$$\begin{aligned} \rho_n &= |\mathbf{x}_{T,n} - \mathbf{x}_{I,n}| + |\mathbf{x}_{R,n} - \bar{\mathbf{x}}_{I,n}| \\ &\quad + \frac{c_w}{c_{\text{sed}}}(|\mathbf{x} - \mathbf{x}_{I,n}| + |\mathbf{x} - \bar{\mathbf{x}}_{I,n}|), \end{aligned} \tag{4.5}$$

which is computed based on assumed sediment parameter values. These may be viewed then as fitting parameters, along with the target vertical coordinate z_S, that may be tuned, e.g., for optimal image focus. The amplitude factor (4.3) may be left unchanged for shallow targets—the key dependence is in the phase.

The sum over transmitter–receiver pairs enhances returns with matching path length over all such pairs. The direct specular reflection occurs at a different surface point for each such pair, and so leads to a reduced signal.

In Fig. 8 we show slices through the image cube generated by the same target model as in Fig. 6. The sediment surface is at 2.5 m depth, and the image is backprojected to the true 3 m target depth using (4.5). The the resonant feature "hot spots" are again evident for the stronger peaks. The direct reflection from the sediment surface is not yet included in the signal. It is likely that sediment heterogeneity (inhomogeneous, or poorly estimated, c_{sed}) and surface roughness will lead to a more defocused image with real data, but for the expected shallow buried targets this should not be a major problem. In fact, we find that backprojecting using the water column form (4.2) still produces good images (mainly because the sediment and water sound speeds differ by less than 15%). This is, in fact, likely the best strategy when surveying areas with little or no prior sediment knowledge.

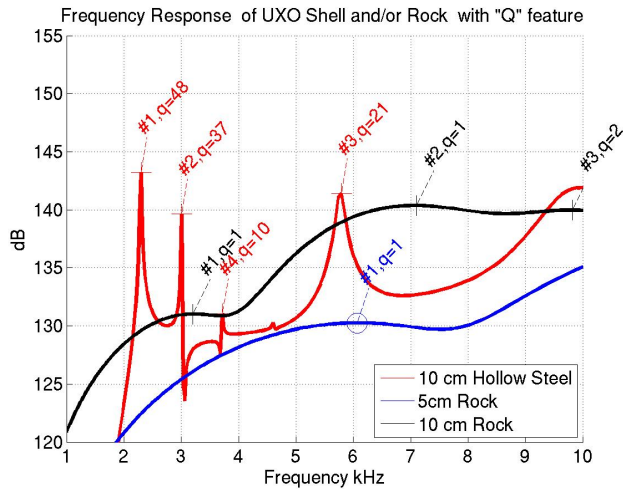

FIG. 10: Spectral responses at the target positions, together with extracted resonant peak characteristics based on a Lorentzian fit (5.1), about the neighborhood of each local maximum f_0. The quality factor Q-values for the hollow shell are at least an order of magnitude larger than those for the solid targets. The latter do not even correspond to true resonances, which all lie outside the plotted frequency band, but to broad maxima in the variation of the scattering response.

V. RESONANCE-BASED FEATURE EXTRACTION AND DETECTION METRICS

We end the main part of this report with a simulation study that combines the essential physics of the previous analysis with an illustration of a basic target feature extraction and discrimination algorithm that is based on reasonable assumptions about the rough statistical character of the classes of targets and clutter that might be encountered.

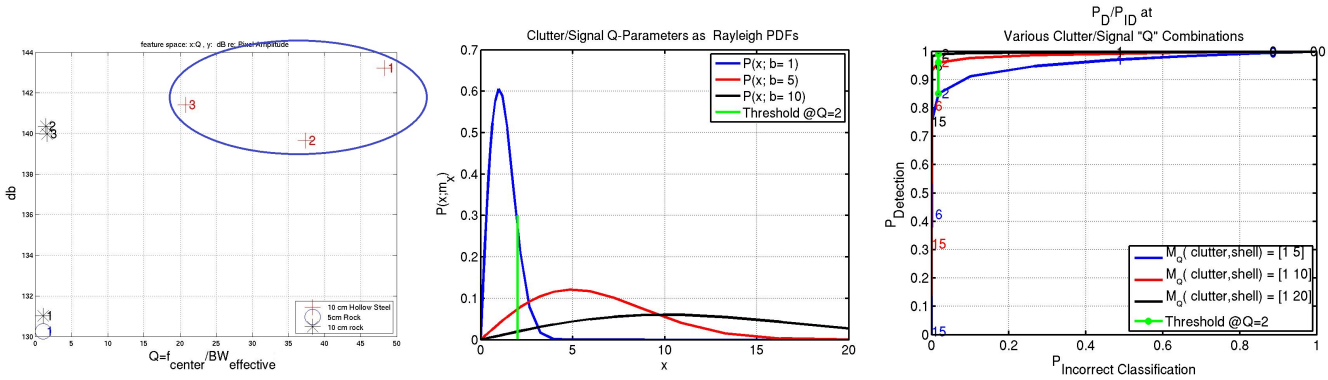

FIG. 11: **Left:** Plot of peak characteristics, labeled in Fig. 10, in the A_0-Q feature space. The essential hollow target discriminator is seen to be the much larger Q-values (circled points) compared to those of solid targets. We expect this to remain robust, even if reduced somewhat by real world effects (e.g., sensor dynamic range, actual UXO target geometries, intrinsic dissipation). **Center:** Statistical spread of target Q-values modeled, for illustration purposes, as a Rayleigh distribution with the given mean b. The true distribution will be strongly site dependent, and characterized through future data collects. **Right:** ROC curves (detection vs. false alarm probability as a function of threshold) derived from this statistical model using $b_{\rm cltr} = 1$ and $b_{\rm UXO} = 5, 10, 20$. Annotations show the threshold value $Q_{\rm thr}$ at various points along the curves.

The previous analysis presented closed form solutions for scattering from sediment emplaced objects, such as elastic shells and naturally occurring clutter. In particular, rocks of various sizes form the most challenging clutter case (and the primary motivation for this work) in that (1) their spatially localized returns (of similar size to a UXO) are routinely confused with underwater UXO, and (2) the relatively homogenous sediment does not provide nearly the same return intensity per unit volume. In Fig. 9 we show 2D spatial slices of the holographic image, at a sequence of frequencies corresponding to the shell resonances, created using four buried targets—two shells and two "rocks".

A. Feature extraction

The first point to note as that the image resolution is more than sufficient, at this physically reasonable 3 m vertical standoff, to individually localize the targets. This localization is critical because it is the basis for isolating individual target spectral responses. The latter, in the form of the frequency dependence at the target pixel, are shown in Fig. 10. The contrast between the multi-peaked, resonant response of the hollow shell, and the smooth solid target response, is abundantly clear in the low frequency band of interest. We quantify these differences by performing a Lorentzian fit

$$|S(f)| \approx \frac{A_0}{Q^2(f/f_0 - 1)^2 + 1} \tag{5.1}$$

in the neighborhood of each local maximum f_0. The results are annotated on the plot. The hollow shell quality factor values (inverse relative peak widths Q) are seen to be at least an order of magnitude larger for the shell. This physical characteristic has been noted in previous work [2, 3], and forms the basis for our discrimination algorithm.

Figure 11 demonstrates the significant discrimination power of this resonance based feature. In the left panel we plot these extracted features in the (A_0, Q) plane. The key discriminator is again seen to be Q, and classifying a target as a shell is then based simply on drawing a vertical line at some threshold value of Q (e.g., $Q_{\rm thr} = 2$), and declaring all targets to the left of it as clutter, and all targets to the right as UXO-like shells.

B. ROC curve and detection metrics

Feature extraction from real survey data with many targets will lead to much more populous clusters of points. Based on the previously described physics, however we expect two reasonably separated clusters, one at larger Q due to UXO shells in the size range of interest, and one at much smaller Q due to rocks of various sizes. The separation will not necessarily be perfect: (1) There could be smaller, thicker UXO present with unusually high resonant frequencies above 10 kHz, and are therefore either not detected at all or are mistaken for rocks, or (2) there could be larger, or more highly compressible, rocks with sharp resonances below 10 kHz that are then mistaken for UXO.

This uncertainty, leading to missed detections and false alarms, may be quantified statistically using a ROC curve, illustrated in center and right panels of Fig. 11. The UXO and clutter point clusters are assumed to be described by distributions $p_{\rm UXO}(Q)$, and $p_{\rm cltr}(Q)$, respectively. These are, in general, site characteristic, and depend on the distribution of rock sizes, UXO sizes and types, etc. Thus, for example, if UXO items are metal shells with some range of sizes, geometries, material types, inner and outer radii, etc., lying in sediment

characterized as well by some distribution of density and sound speed, then the result of a measurement will be a response curve similar in character to the hollow target curve in Fig. 10, but with a different distribution of resonance peaks depending on the exact target. Similarly, the clutter items will be represented by a distribution of solid rock (or perhaps other man made item) sizes, geometries, and surrounding sediment properties. The result of the feature extraction algorithm will be a set of points different from those in the left panel of Fig. 11, but still strongly distinguished in Q.

The detection probability $P_{\rm D}(Q_{\rm thr})$ depends on the chosen threshold, and is defined by the area under $p_{\rm UXO}(Q)$ for $Q > Q_{\rm thr}$ (and the missed detections are quantified by the complementary area under $Q < Q_{\rm thr}$). Similarly, the false alarm probability $P_{\rm FA}(Q_{\rm thr})$ is defined by the area under $p_{\rm cltr}(Q)$ for $Q > Q_{\rm thr}$.

Purely for illustrative purposes, suppose that $p_{\rm cltr}(Q)$, $p_{\rm UXO}(Q)$ are modeled as simple Rayleigh distributions

$$p_R(x;\sigma) = (x/\sigma^2)e^{-x^2/2\sigma^2}, \tag{5.2}$$

characterized by two different values of the mean $b = \sigma\sqrt{\pi/2}$. The choices $b = 1, 5, 10$ are shown in the center panel of Fig. 11. The Rayleigh choice is actually likely quite conservative, as the spread in Q for $b_{\rm UXO} = 10, 20$ is much broader than actually suggested by either our physics analysis or earlier data collects. Thus, the illustrated distributions assumed likely overstate both the probability of a UXO having a broad, rock-like response as well as the probability that a rock will having a narrow UXO-like response. Using $b_{\rm cltr} = 1$ for the clutter, the resulting ROC curve (plot of $P_{\rm D}$ vs. $P_{\rm FA}$ as $Q_{\rm thr}$ is varied) is shown in the right panel of Fig. 11 for the three different UXO distribution choices, $b_{\rm UXO} = 5, 10, 20$. Using $Q_{\rm thr} = 2$ the false alarm rate is below 2%, and the detection rate is above 85%.

Although the true distributions $p_{\rm UXO}$ and $p_{\rm cltr}$ for a given UXO survey area will likely differ substantially from the Rayleigh choices, the results in Fig. 11—especially the robust separation in Q between UXO and clutter, and well informed estimates of their expected values—are nevertheless derived from the essential physics of our models.

C. Conclusions

In designing our physics-based model and holographic image-based target detection and discrimination algorithm, we have attempted to capture as accurately as possible the key physical features of the sensor parameters, measurement grid geometry, water and sediment acoustic propagation characteristics, and target elastic response. Certain elements can be captured only qualitatively (e.g., realistic UXO resonant responses), but given the correctness of the basic physics, we do not believe that this will affect the key conclusions of the analysis. Thus, by focusing on the 3–10 kHz sediment-penetrating frequency range, we expect physical buried UXO-sized shells to indeed exhibit sharp resonant features, with $Q \gtrsim 10$ (and this is supported by some existing data [2, 3]), in strong contrast to typical clutter responses with $Q \lesssim 1$.

Thus, with sufficiently high quality, geolocated data, lying within the capabilities of a carefully fielded BOSS platform, the illustrative ROC curves shown in Fig. 11 may even represent *conservative* estimates of the ultimate UXO discrimination capability of such a system.

APPENDIX A: BASIS FUNCTIONS FOR A SPHERICAL SHELL

1. Spherical harmonic expansion

In this appendix we construct exact solutions to (2.4) for spherical geometries, using a basis function expansion in vector spherical harmonics. These are analogous to plane waves in horizontally stratified media. The vector harmonics $\mathbf{X}_{lm}(\theta,\phi)$ are constructed from the usual scalar harmonics $Y_{lm}(\theta,\phi)$ via the relation [10]

$$\begin{aligned}\mathbf{X}_{lm} &= \frac{1}{\sqrt{l(l+1)}}\hat{\mathbf{L}}Y_{lm} \\ &= \frac{1}{\sqrt{l(l+1)}}\left[\frac{1}{2}c_{lm}Y_{l,m+1} + \frac{1}{2}c_{l,-m}Y_{l,m-1},\right. \\ &\qquad \left.\frac{1}{2i}c_{lm}Y_{l,m+1} - \frac{1}{2i}c_{l,-m}Y_{l,m-1},\ mY_{lm}\right]\end{aligned} \tag{A1}$$

in which $c_{lm} = \sqrt{(l-m)(l+m+1)}$, and the angular momentum operator

$$\begin{aligned}\hat{\mathbf{L}} &= -i\mathbf{r}\times\nabla \\ &= -i\hat{\boldsymbol{\phi}}\partial_\theta + i\hat{\boldsymbol{\theta}}\frac{1}{\sin(\theta)}\partial_\phi\end{aligned} \tag{A2}$$

depends only on θ, ϕ and derivatives with respect to them [10, 11]. It follows that

$$\hat{\mathbf{r}}\cdot\mathbf{X}_{lm} = 0, \quad \nabla\cdot\mathbf{X}_{lm} = 0. \tag{A3}$$

Note that $X_{00} = 0$: the vector harmonics are defined only for $l \geq 1$.

At fixed frequency ω, the *longitudinal basis functions* are given, for each l, m (including $l = 0$), by

$$\mathbf{s}_L = \frac{1}{k_L}\nabla[z_l(k_L r)Y_{lm}], \tag{A4}$$

in which $k_L = \omega/c_L$ and $z_l(x)$ is a spherical Bessel function [10, 11] satisfying the defining equation

$$z_l'' + \frac{2}{x}z_l' + \left[1 - \frac{l(l+1)}{x^2}\right]z_l = 0. \tag{A5}$$

They are related to the usual cylindrical Bessel functions by $z_l(x) = \sqrt{\pi/2x}Z_{l+1/2}(x)$. In what follows, the regular

Bessel function $j_l(x)$ and outgoing wave Hankel function $h_l^{(1)}(x)$ will be substituted. The harmonic form $\mathbf{s}_L e^{-i\omega t}$ satisfies (A5).

The two *transverse basis functions* are given by

$$\begin{aligned} \mathbf{s}_{T,1} &= z_l(k_T r)\mathbf{X}_{lm} \\ \mathbf{s}_{T,2} &= \frac{1}{k_T}\nabla\times[z_l(k_T r)\mathbf{X}_{lm}], \end{aligned} \tag{A6}$$

for $l \geq 1$, in which $k_T = \omega/c_T$. From the relations

$$\begin{aligned} \nabla\cdot\mathbf{s}_{T,\alpha} &= 0 \\ \frac{1}{k_T}\nabla\times\mathbf{s}_{T,2} &= -\frac{1}{k_T^2}\nabla^2\mathbf{s}_{T,1} = \mathbf{s}_{T,1} \end{aligned} \tag{A7}$$

it follows that the harmonic forms $\mathbf{s}_{T,\alpha}e^{-i\omega t}$ satisfy (A4).

The additional identities required to manipulate these expressions are as follows. The gradient operator may be decomposed into radial and angular components

$$\nabla = \hat{\mathbf{r}}\frac{\partial}{\partial r} - \frac{i}{r}\hat{\mathbf{r}}\times\hat{\mathbf{L}}, \tag{A8}$$

and it follows that for any function $f(r)$ of the radial coordinate only,

$$\nabla[f(r)Y_{lm}] = \hat{\mathbf{r}}(\partial_r f)Y_{lm} - i\sqrt{l(l+1)}\frac{f}{r}\hat{\mathbf{r}}\times\mathbf{X}_{lm}. \tag{A9}$$

Similarly, one obtains

$$\nabla\times[f(r)\mathbf{X}_{lm}] = i\sqrt{l(l+1)}\hat{\mathbf{r}}\frac{f}{r}Y_{lm} + \frac{1}{r}\partial_r(rf)\hat{\mathbf{r}}\times\mathbf{X}_{lm}. \tag{A10}$$

Similar to the fact that the set of scalar harmonics $\{Y_{lm}\}$ form an orthonormal basis for scalar functions on the unit sphere, the set of locally orthogonal vector pairs $\{\mathbf{X}_{lm}, \hat{\mathbf{r}}\times\mathbf{X}_{lm}\}$ form an orthonormal basis for transverse vector fields on the unit sphere [10].

Using (A9) and (A10) one may write out the basis functions explicitly in the form

$$\begin{aligned} \mathbf{s}_L &= \hat{\mathbf{r}}z_l'(x_L)Y_{lm} - i\sqrt{l(l+1)}\frac{z_l(x_L)}{x_L}\hat{\mathbf{r}}\times\mathbf{X}_{lm} \\ \mathbf{s}_{T,1} &= z_l(x_T)\mathbf{X}_{lm} \\ \mathbf{s}_{T,2} &= i\sqrt{l(l+1)}\hat{\mathbf{r}}\frac{z_l(x_T)}{x_T}Y_{lm} + \frac{[x_T z_l(x_T)]'}{x_T}\hat{\mathbf{r}}\times\mathbf{X}_{lm}, \end{aligned} \tag{A11}$$

in which we have defined $x_\alpha = k_\alpha r$, and the primes indicate differentiation with respect to one these arguments, as appropriate from context.

2. Traction boundary condition inputs

Using (A2), the required radial traction is given by

$$\begin{aligned} \hat{\mathbf{r}}\cdot\hat{\boldsymbol{\tau}} &= \lambda\hat{\mathbf{r}}\nabla\cdot\mathbf{s} + \mu[(\hat{\mathbf{r}}\cdot\nabla)\mathbf{s} + (\nabla\mathbf{s})\cdot\hat{\mathbf{r}}] \\ &= \lambda\hat{\mathbf{r}}\nabla\cdot\mathbf{s} + \mu\left[\partial_r\mathbf{s} + \nabla(\mathbf{s}\cdot\hat{\mathbf{r}}) - \frac{1}{r}(\mathbb{1} - \hat{\mathbf{r}}\hat{\mathbf{r}})\mathbf{s}\right]. \end{aligned} \tag{A12}$$

Substituting (A11), the required inputs to the boundary conditions are as follows. (a) Divergence term:

$$\begin{aligned} \frac{1}{k_L}\nabla\cdot\mathbf{s}_L &= \frac{1}{k_L^2}\nabla^2[z_l(x_L)Y_{lm}] = -z_l(x_L)Y_{lm} \\ \nabla\cdot\mathbf{s}_{T,\alpha} &= 0. \end{aligned} \tag{A13}$$

The first line follows from the fact that $z_l(x_L)Y_{lm}$ is a solution to the Helmholtz equation, $(\nabla^2 + k_L^2)\phi = 0$. (b) Radial derivative term:

$$\begin{aligned} \frac{1}{k_L}\partial_r\mathbf{s}_L &= \hat{\mathbf{r}}z_l''(x_L)Y_{lm} \\ &\quad - i\sqrt{l(l+1)}\left[\frac{z_l(x_L)}{x_L}\right]'\hat{\mathbf{r}}\times\mathbf{X}_{lm} \\ \frac{1}{k_T}\partial_r\mathbf{s}_{T,1} &= z_l'(x_T)\mathbf{X}_{lm} \\ \frac{1}{k_T}\partial_r\mathbf{s}_{T,2} &= i\sqrt{l(l+1)}\hat{\mathbf{r}}\left[\frac{z_l(x_T)}{x_T}\right]'Y_{lm} \\ &\quad + \left\{\frac{[x_T z_l(x_T)]'}{x_T}\right\}'\hat{\mathbf{r}}\times\mathbf{X}_{lm}. \end{aligned} \tag{A14}$$

In what follows, the Bessel function second derivatives will ultimately be expressed in terms of lower order derivatives using the defining equation (A5). (c) Gradient of radial component term:

$$\begin{aligned} \frac{1}{k_L}\nabla(\mathbf{s}_L\cdot\hat{\mathbf{r}}) &= \frac{1}{k_L}\nabla[z_l'(x_L)Y_{lm}] \\ &= \hat{\mathbf{r}}z_l''(x_L)Y_{lm} \\ &\quad - i\sqrt{l(l+1)}\frac{z_l'(x_L)}{x_L}\hat{\mathbf{r}}\times\mathbf{X}_{lm} \\ \frac{1}{k_T}\nabla(\mathbf{s}_{T,1}\cdot\hat{\mathbf{r}}) &= 0 \\ \frac{1}{k_T}\nabla(\mathbf{s}_{T,2}\cdot\hat{\mathbf{r}}) &= i\sqrt{l(l+1)}\frac{1}{k_T}\nabla\left[\frac{z_l(x_T)}{x_T}Y_{lm}\right] \\ &= i\sqrt{l(l+1)}\hat{\mathbf{r}}\left[\frac{z_l(x_T)}{x_T}\right]'Y_{lm} \\ &\quad + l(l+1)\frac{z_l(x_T)}{x_T^2}\hat{\mathbf{r}}\times\mathbf{X}_{lm}. \end{aligned} \tag{A15}$$

(d) Transverse projection term (which simply suppresses the $\hat{\mathbf{r}}Y_{lm}$ term in each basis function):

$$\begin{aligned} (\mathbb{1} - \hat{\mathbf{r}}\hat{\mathbf{r}})\mathbf{s}_L &= -i\sqrt{l(l+1)}\frac{z_l(x_L)}{x_L}\hat{\mathbf{r}}\times\mathbf{X}_{lm} \\ (\mathbb{1} - \hat{\mathbf{r}}\hat{\mathbf{r}})\mathbf{s}_{T,1} &= \mathbf{s}_{T,1} = z_l(x_T)\mathbf{X}_{lm} \\ (\mathbb{1} - \hat{\mathbf{r}}\hat{\mathbf{r}})\mathbf{s}_{T,2} &= \frac{[x_T z_l(x_T)]'}{x_T}\hat{\mathbf{r}}\times\mathbf{X}_{lm}. \end{aligned} \tag{A16}$$

The key point to note here is that all of these terms are superpositions of $\hat{\mathbf{r}}Y_{lm}, \mathbf{X}_{lm}, \hat{\mathbf{r}}\times\mathbf{X}_{lm}$, and hence remain diagonal in the space defined by fixed values of the angular momentum indices l, m: the boundary conditions do not mix different spherical harmonic orders (although

they do mix the three different polarizations). Assembling all of the terms, one obtains

$$\begin{aligned}
\frac{1}{k_L}\hat{\mathbf{r}}\cdot\hat{\boldsymbol{\tau}}_L &= [2\mu z_l''(x_L) - \lambda z_l(x_L)]\,\hat{\mathbf{r}}Y_{lm} \\
&\quad - 2i\mu\sqrt{l(l+1)}\left[\frac{z_l(x_L)}{x_L}\right]'\hat{\mathbf{r}}\times\mathbf{X}_{lm} \\
\frac{1}{k_T}\hat{\mathbf{r}}\cdot\hat{\boldsymbol{\tau}}_{T,1} &= \mu x_T\left[\frac{z_l(x_T)}{x_T}\right]'\mathbf{X}_{lm} \qquad \text{(A17)} \\
\frac{1}{k_T}\hat{\mathbf{r}}\cdot\hat{\boldsymbol{\tau}}_{T,2} &= 2i\mu\sqrt{l(l+1)}\left[\frac{z_l(x_T)}{x_T}\right]'\hat{\mathbf{r}}Y_{lm} \\
&\quad + \mu\left[z_l''(x_T) + (l+2)(l-1)\frac{z_L(x_T)}{x_T^2}\right]\hat{\mathbf{r}}\times\mathbf{X}_{lm}.
\end{aligned}$$

In addition to (A5), the recursion relations

$$\begin{aligned}
z_l'(x) &= \frac{1}{2l+1}[l z_{l-1}(x) - (l+1)z_{l+1}(x)] \\
\frac{z_l(x)}{x} &= \frac{1}{2l+1}[z_{l-1}(x) + z_{l+1}(x)] \qquad \text{(A18)}
\end{aligned}$$

are useful for simplifying expressions for numerical implementation.

APPENDIX B: SOLUTIONS TO THE ELASTIC EQUATIONS WITH SPHERICAL GEOMETRY

The general approach to constructing solutions in a spherical geometry, comprised of N concentric spherical shells, is to expand $\mathbf{s}$ in each shell $j = 1, 2, \ldots, N$ in the form

$$\begin{aligned}
\mathbf{s}(\mathbf{r}) &= A_j\mathbf{s}_L[j_l(x_L^j)] + B_j\mathbf{s}_L[h_l^{(1)}(x_T^j)] + C_j\mathbf{s}_{T,1}[j_l(x_T^j)] \\
&\quad + D_j\mathbf{s}_{T,1}[h_l^{(1)}(x_T^j)] + E_j\mathbf{s}_{T,2}[j_l(x_T^j)] \\
&\quad + F_j\mathbf{s}_{T,2}[h_l^{(1)}(x_T^j)], \quad a_{j-1} \le r < a_j, \qquad \text{(B1)}
\end{aligned}$$

where the notation indicates the Bessel function form to be substituted for z_l in (A4) or (A11), and $x_\alpha^j = k_\alpha^j r = (\omega/c_\alpha^j)r$, where c_α^j are the sound speeds in shell j with outer radius a_j. We define $a_0 = 0$ (innermost shell is a sphere of radius a_1) and $a_N = \infty$ (outermost shell is an infinite background). Regularity at the origin, $r = 0$, requires $D_1 = E_1 = F_1 = 0$, and any fluid layer requires $B_j = C_j = E_j = F_j = 0$.

We will assume that the system is driven by an incident transmitted wave $\mathbf{s}_{\rm in}$ in the background, with a *known* expansion

$$\begin{aligned}
\mathbf{s}_{\rm in}(\mathbf{r}) &= \sum_{l,m}\left\{A_{lm}\mathbf{s}_L[j_l(x_L^N)] + C_{lm}\mathbf{s}_{T,1}[j_l(x_T^N)]\right. \\
&\quad \left. + E_{lm}\mathbf{s}_{T,2}[j_l(x_T^N)]\right\} \qquad \text{(B2)}
\end{aligned}$$

in the neighborhood of the target.

For example, a plane wave has the expansion [10, 11]

$$e^{i\mathbf{k}\cdot\mathbf{x}} = 4\pi\sum_{l,m} i^l j_l(kr)Y_{lm}^*(\theta',\phi')Y_{lm}(\theta,\phi), \qquad \text{(B3)}$$

where θ', ϕ' define the polar angles of the wavevector $\mathbf{k}$. Using $\hat{\mathbf{k}}e^{i\mathbf{k}\cdot\mathbf{x}} = -(i/k)\nabla e^{i\mathbf{k}\cdot\mathbf{x}}$ and (A4), one obtains the expansion of a longitudinal wave. Alternatively, for a spherical wave originating from $\mathbf{x}'$ one obtains

$$\frac{e^{ik|\mathbf{x}-\mathbf{x}'|}}{4\pi|\mathbf{x}-\mathbf{x}'|} = ik\sum_{l,m} j_l(kr_<)h_l^{(1)}(kr_>)Y_{lm}^*(\theta',\phi')Y_{lm}(\theta,\phi), \qquad \text{(B4)}$$

where $r_> = \max\{r, r'\}$, $r_< = \min\{r, r'\}$, and the longitudinal wave solution is again given by $-(i/k)\nabla$ acting on both sides. Somewhat more complicated manipulations produce vector harmonic expansions for transverse polarized waves [10]. However, in all that follows we will consider only a fluid background, and (B3), (B4) then suffice.

For each l, m one then substitutes A_{lm}, C_{lm}, E_{lm} for A_N, C_N, E_N in (B1), which then produces the mathematically consistent problem of $6(N-1)$ equations (one for each of the 6 boundary conditions at each shell boundary $a_1, a_2, \ldots, a_{N-1}$) in $6(N-1)$ unknowns. These two numbers are reduced appropriately if there are fluid layers, but remain equal.

1. Elastic shell in a fluid background

We consider now the specific problem of a single elastic shell with fluid void and background. The mode expansion (B1) in the fluid regions takes the explicit form

$$\mathbf{s}(\mathbf{r}) = \begin{cases} A_1\mathbf{s}_L[j_l(x_L^1)], & r < b \\ \mathbf{s}_L[j_l(x_L^3)] + B_3\mathbf{s}_L[h_l^{(1)}(x_L^3)], & r \ge a \end{cases} \qquad \text{(B5)}$$

where we have defined $a_1 = b$ and $a_2 = a$ and normalized $A_3 = 1$ as the known excitation coefficient. For $b < r \le a$ all six terms are present.

Continuity of $\mathbf{s}\cdot\hat{\mathbf{r}}$ at $r = a, b$ involves only the matching of the $\hat{\mathbf{r}}Y_{lm}$ coefficients, and yields the two equations

$$
\begin{aligned}
0 &= -A_1 j_l'(b_L^1) + A_2 j_l'(b_L) + B_2 h_l^{(1)\prime}(b_L) + \frac{i\sqrt{l(l+1)}}{b_T}\left[E_2 j_l(b_T) + F_2 h_l^{(1)}(b_T)\right] \\
j_l'(a_L^3) &= A_2 j_l'(a_L) + B_2 h_l^{(1)\prime}(a_L) + \frac{i\sqrt{l(l+1)}}{a_T}\left[E_2 j_l(a_T) + F_2 h_l^{(1)}(a_T)\right] - B_3 h_l^{(1)\prime}(a_L^3).
\end{aligned} \tag{B6}
$$

where $b_\alpha^j = k_\alpha^j b$, $a_\alpha^j = k_\alpha^j a$, except that, for the remainder of this section, to avoid notational clutter we will drop the label index '2' on all elastic shell quantities: $\mu_2 = \mu$, $\lambda_2 = \lambda$, $a_L^2 = a_L$, $b_L^2 = b_L$, etc.

Continuity of the traction yields three equations at each boundary, one each for the independent coefficients of $\hat{\mathbf{r}} Y_{lm}, \mathbf{X}_{lm}, \hat{\mathbf{r}} \times \mathbf{X}_{lm}$. Since $\mu_1 = \mu_3 = 0$, from (A16), only longitudinal terms appear in the fluid regions, and these produce the pair of equations

$$
\begin{aligned}
0 &= A_1 \lambda_1 b_L^1 j_l(b_L^1) + A_2 b_L \left[2\mu j_l''(b_L) - \lambda j_l(b_L)\right] + B_2 b_L \left[2\mu h_l^{(1)\prime\prime}(b_L) - \lambda h_l^{(1)}(b_L)\right] \\
&\quad + 2i\mu\sqrt{l(l+1)} b_T \left\{ E_2 \left[\frac{j_l(b_T)}{b_T}\right]' + F_2 \left[\frac{h_l^{(1)}(b_T)}{b_T}\right]' \right\} \\
-\lambda_3 a_L^3 j_l(a_L^3) &= A_2 a_L \left[2\mu j_l''(a_L) - \lambda j_l(a_L)\right] + B_2 a_L \left[2\mu h_l^{(1)\prime\prime}(a_L) - \lambda h_l^{(1)}(a_L)\right] \\
&\quad + 2i\mu\sqrt{l(l+1)} a_T \left\{ E_2 \left[\frac{j_l(a_T)}{a_T}\right]' + F_2 \left[\frac{h_l^{(1)}(a_T)}{a_T}\right]' \right\} + B_3 \lambda_3 a_L^3 h_l^{(1)}(a_L^3)
\end{aligned} \tag{B7}
$$

On the other hand, the transverse terms are completely absent in the fluid region, and the other four equations therefore involve only the coefficients in the elastic shell. The continuity of the $\mathbf{X}_{lm}$ terms yields the pair

$$
0 = C_2 \left[\frac{j_l(b_T)}{b_T}\right]' + D_2 \left[\frac{h_l^{(1)}(b_T)}{b_T}\right]', \quad 0 = C_2 \left[\frac{j_l(a_T)}{a_T}\right]' + D_2 \left[\frac{h_l^{(1)}(a_T)}{a_T}\right]' \tag{B8}
$$

while continuity of the $\hat{\mathbf{r}} \times \mathbf{X}_{lm}$ terms yields the pair

$$
\begin{aligned}
0 &= -2i\sqrt{l(l+1)} b_L \left\{ A_2 \left[\frac{j_l(b_L)}{b_L}\right]' + B_2 \left[\frac{h_l^{(1)}(b_L)}{b_L}\right]' \right\} \\
&\quad + E_2 \left[b_T j_l''(b_T) + (l+2)(l-1)\frac{j_l(b_T)}{b_T}\right] + F_2 \left[b_T h_l^{(1)\prime\prime}(b_T) + (l+2)(l-1)\frac{h_l^{(1)}(b_T)}{b_T}\right] \\
0 &= -2i\sqrt{l(l+1)} a_L \left\{ A_2 \left[\frac{j_l(a_L)}{a_L}\right]' + B_2 \left[\frac{h_l^{(1)}(a_L)}{a_L}\right]' \right\} \\
&\quad + E_2 \left[a_T j_l''(a_T) + (l+2)(l-1)\frac{j_l(a_T)}{a_T}\right] + F_2 \left[a_T h_l^{(1)\prime\prime}(a_T) + (l+2)(l-1)\frac{h_l^{(1)}(a_T)}{a_T}\right]
\end{aligned} \tag{B9}
$$

Recall that for $l = 0$ only the longitudinal terms are present. Equations (B6) and (B7) then determine A_1, A_2, B_2, B_3, and equation (B9) becomes vacuous.

It is apparent that C_2, D_2, appearing only in (B8), are completely decoupled from the rest of the system. The solution to (B8) is $C_2 = D_2 = 0$, except at certain eigenfrequencies where the corresponding determinant

$$
\begin{aligned}
\mathcal{D}_{T,1}(\omega) &= \left[\frac{j_l(b_T)}{b_T}\right]' \left[\frac{h_l^{(1)}(a_T)}{a_T}\right]' \\
&\quad - \left[\frac{h_l^{(1)}(b_T)}{b_T}\right]' \left[\frac{j_l(a_T)}{a_T}\right]'
\end{aligned} \tag{B10}
$$

vanishes. Thus, only the L and T_2 modes are excited by the incident wave. The T_1 shear mode lives completely inside the elastic shell, and will be present only if the eigenmodes have been previously excited, and live on in-

definitely in this dissipation free model. In the presence of dissipation, these will die away, and we may simply take $C_2 = D_2 = 0$.

The remaining six coefficients $\mathbf{A} \equiv [A_1, A_2, B_2, E_2, F_2, B_3]^T$ are then determined (B6), (B7), and (B9), which may be represented in the matrix form

$$\hat{\mathcal{M}}(a,b)\mathbf{A} = \mathbf{V}, \tag{B11}$$

in which the matrix entries may be read off from these three equations (in the order written):

$$\hat{\mathcal{M}}(a,b) = \begin{bmatrix} -J_1(b_L^1) & J_1(b_L) & H_1(b_L) & J_2(b_T) & H_2(b_T) & 0 \\ 0 & J_1(a_L) & H_1(a_L) & J_2(a_T) & H_2(a_T) & -H_1(a_L^3) \\ -J_6(b_L^1) & J_3(b_L) & H_3(b_L) & J_4(b_T) & H_4(b_T) & 0 \\ 0 & J_3(a_L) & H_3(a_L) & J_4(a_T) & H_4(a_T) & -H_7(a_L^3) \\ 0 & -J_4(b_L) & -H_4(b_L) & J_5(b_T) & H_5(b_T) & 0 \\ 0 & -J_4(a_L) & -H_4(a_L) & J_5(a_T) & H_5(a_T) & 0 \end{bmatrix}, \quad \mathbf{V} = \begin{bmatrix} 0 \\ J_1(a_L^3) \\ 0 \\ J_7(a_L^3) \\ 0 \\ 0 \\ 0 \end{bmatrix}, \tag{B12}$$

where we define

$$\begin{aligned} J_1(x) &= j_l'(x), \quad J_2(x) = i\sqrt{l(l+1)}j_l(x)/x, \quad J_3(x) = x[2\mu j_l''(x) - \lambda j_l(x)] \\ H_1(x) &= h_l^{(1)\prime}(x), \quad H_2(x) = i\sqrt{l(l+1)}h_l^{(1)}(x)/x, \quad H_3(x) = x[2\mu h_l^{(1)\prime\prime}(x) - \lambda h_l^{(1)}(x)] \\ J_4(x) &= 2i\mu\sqrt{l(l+1)}x[j_l(x)/x)]', \quad J_5(x) = \mu x\left[j_l''(x) + (l+2)(l-1)j_l(x)/x^2\right] \\ H_4(x) &= 2i\mu\sqrt{l(l+1)}x[h_l^{(1)}(x)/x)]', \quad H_5(x) = \mu x\left[h_l^{(1)\prime\prime}(x) + (l+2)(l-1)h_l^{(1)}(x)/x^2\right] \\ J_6(x) &= -\lambda_1 x j_l(x), \quad J_7(x) = -\lambda_3 x j_l(x), \quad H_7(x) = -\lambda_3 x h_l^{(1)}(x) \end{aligned} \tag{B13}$$

Note that if one sets $\lambda_1 = \lambda_3 = 0$, then A_1, B_3 and the driving term drop out of (B7). Equations (B7) and (B9) then become homogeneous equations for A_2, B_2, E_2, F_2 (represented by the 4×4 block consisting of the last four rows and central four columns of $\mathcal{M}$), whose solution must be zero unless the corresponding determinant vanishes. This limit corresponds to free ringing modes of the shell. The coefficients A_1, B_3 are determined by (B6) (with the driving term dropped) in terms of the (arbitrary) shell mode amplitudes. To obtain sensible solutions, one should take both $\lambda_1, \lambda_3 \to 0$ and $\rho_1, \rho_2 \to 0$ in such a way that their ratio in c_L^1, c_L^3 remains finite. One is then taking the limit of a very dilute background fluid which has negligible effect on the now freely oscillating (and non-radiating) elastic modes of the shell.

2. Special cases

We Consider now some limiting cases where analytic results can be obtained. We will focus mainly on the free ringing modes, defined by equations (B7) and (B9) with $\lambda_1 = \lambda_3 = 0$.

a. *Solid elastic sphere*

First consider the solid elastic sphere limit, $b = 0$. Regularity at the origin then requires that $B_2 = F_2 = 0$, and the boundary conditions at $r = a$ [second of each of equations (B6), (B7) and (B9)] reduce to the matrix equation

$$\begin{bmatrix} J_1(a_L) & J_2(a_L) & -H_1(a_L^3) \\ J_3(a_L) & J_4(a_T) & -H_7(a_L^3) \\ -J_4(a_L) & J_5(a_T) & 0 \end{bmatrix} \begin{bmatrix} A_2 \\ E_2 \\ B_3 \end{bmatrix} = \begin{bmatrix} J_1(a_L^3) \\ J_7(a_L^3) \\ 0 \end{bmatrix}. \tag{B14}$$

The vanishing of the corresponding determinant

$$\mathcal{D}^{\rm sph}(\omega) = J_3(a_L)J_5(a_T) + J_4(a_L)J_4(a_T), \tag{B15}$$

constructed from the last two rows of (B14), yields the free mode frequencies. For $l = 0$, E_2 is absent, and the second row of (B14) produces the constraint $J_3(a_L) = 0$, i.e.,

$$2\mu j_l''(a_L) - \lambda j_l(a_L) = 0. \tag{B16}$$

For $\mu = 0$ this reduces to the usual fluid acoustic "pressure release" boundary condition $j_0(a_L) = 0$. The exact relation $j_0(x) = \sin(x)/x$, then implies

$$\frac{\tan(a_L)}{a_L} = \frac{4\mu}{4\mu - (\lambda + 2\mu)a_L^2} = \frac{1}{1 - (c_L a_L/2c_T)^2}, \tag{B17}$$

which reduces to $a_L = \omega a/c_L = n\pi$, $n \geq 1$, in the fluid limit, $\mu = 0$.

b. *Thin elastic shell*

Next consider the opposite limit of free modes in a very thin elastic shell, $\delta = a - b \ll a$. For $\delta = 0$ many matrix elements of $\hat{\mathcal{M}}(a,a)$ are equal (in particular, the last two rows are identical) and the linear system of equations becomes singular. To obtain sensible results, one must expand the equations to linear order in δ. After some simplifications obtained by subtracting the even rows from the odd rows, one may write the resulting equations in the form

$$\left[\hat{\mathcal{M}}_0(a) + \frac{\delta}{a}\hat{\mathcal{M}}_1(a)\right]\mathbf{A} = \tilde{\mathbf{V}} \tag{B18}$$

in which

$$\hat{\mathcal{M}}_0(a) = \begin{bmatrix} J_1(a_L^1) & 0 & 0 & 0 & 0 & -H_1(a_L^3) \\ 0 & J_1(a_L) & H_1(a_L) & J_2(a_T) & H_2(a_T) & -H_1(a_L^3) \\ J_6(a_L^1) & 0 & 0 & 0 & 0 & -H_7(a_L^3) \\ 0 & J_3(a_L) & H_3(a_L) & J_4(a_T) & H_4(a_T) & -H_7(a_L^3) \\ 0 & -a_L J_4'(a_L) & -a_L H_4'(a_L) & a_T J_5'(a_T) & a_T H_5'(a_T) & 0 \\ 0 & -J_4(a_L) & -H_4(a_L) & J_5(a_T) & H_5(a_T) & 0 \end{bmatrix}, \quad \tilde{\mathbf{V}} = \begin{bmatrix} J_1(a_L^3) \\ J_1(a_L^3) \\ J_7(a_L^3) \\ J_7(a_L^3) \\ 0 \\ 0 \end{bmatrix}$$

$$\hat{\mathcal{M}}_1(a) = \begin{bmatrix} -a_L^1 J_1'(a_L^1) & a_L J_1'(a_L) & a_L H_1'(a_L) & a_T J_2'(a_T) & a_T H_2'(a_T) & 0 \\ 0 & 0 & 0 & 0 & 0 & 0 \\ -a_L^1 J_6'(a_L^1) & a_L J_3'(a_L) & a_L H_3'(a_L) & a_T J_4'(a_T) & a_T H_4'(a_T) & 0 \\ 0 & 0 & 0 & 0 & 0 & 0 \\ 0 & \frac{1}{2}a_L^2 J_4''(a_L) & \frac{1}{2}a_L^2 H_4''(a_L) & -\frac{1}{2}a_T^2 J_5''(a_T) & -\frac{1}{2}a_T^2 H_5''(a_T) & 0 \\ 0 & 0 & 0 & 0 & 0 & 0 \end{bmatrix} \tag{B19}$$

Note that the fifth row was nominally of linear order, but since equations (B9) are homogeneous, δ/a was divided out after the subtraction to generate a new leading order equation. The first order term then requires a second derivative.

The matrix $\mathcal{M}_0$ is invertible, and so can be used to produce leading order results for the coefficients $\mathbf{A}_0 = \mathcal{M}_0^{-1}\tilde{\mathbf{V}}$. The first and third rows provide closed solutions for A_1, B_3,

$$\begin{bmatrix} J_1(a_L) & -H_1(a_L^3) \\ J_6(a_L^1 & -H_7(a_L^3) \end{bmatrix} \begin{bmatrix} A_{1,0} \\ B_{3,0} \end{bmatrix} = \begin{bmatrix} J_1(a_L^3) \\ J_7(a_L^3) \end{bmatrix}. \tag{B20}$$

which are identical to the fluid equations in the absence of the elastic membrane. Thus, the leading order scattered wave arises purely from scattering off the fluid sphere. The membrane then moves passively in response to the fluid motion: this is quantified by the remaining four rows, in which the driving vector $[J_1(a_L^3) + B_3 H_1(a_L^3),\ J_7(a_L^3) + B_3 H_7(a_L^3),\ 0,\ 0]^T$ now includes the known B_3 terms (last column).

There is a subtlety if one chooses $\lambda_1 = \lambda_3$ and $\rho_1 = \rho_3$ (hence $c_L^1 = c_L^3$ and $a_L^1 = a_L^3$) [9]. The two fluids are identical, and there is no scattering: equation (B21) produces $A_1 = 1$ and $B_3 = 0$. To obtain the leading $B_3 = (\delta/a)\tilde{B}_3$ scattering, which is due to the dynamical effect of the membrane, one must include $\mathcal{M}_1$, which yields $\mathbf{A} = \mathbf{A}_0 + (\delta/a)\mathbf{A}_1$ with

$$\mathbf{A}_1 = -\hat{\mathcal{M}}_0^{-1}\hat{\mathcal{M}}_1\mathbf{A}_0. \tag{B21}$$

c. *Thin shell free modes*

Setting $\lambda_1 = \lambda_3 = 0$, hence $J_6 = J_7 = H_7 = 0$, the free shell dynamics is defined by the last four rows, and middle four columns, of $\mathcal{M}$. Since the third row of $\mathcal{M}_0$ vanishes identically in this limit, the third row of $\mathcal{M}_1$ enters at leading order, and the free modes are then determined by the vanishing of the "membrane determinant" of the matrix

$$\hat{\mathcal{M}}_{\rm fs}(a) = \begin{bmatrix} a_L J_3'(a_L) & a_L H_3'(a_L) & a_T J_4'(a_T) & a_T H_4'(a_T) \\ J_3(a_L) & H_3(a_L) & J_4(a_T) & H_4(a_T) \\ -a_L J_4'(a_L) & -a_L H_4'(a_L) & a_T J_5'(a_T) & a_T H_5'(a_T) \\ -J_4(a_L) & -H_4(a_L) & J_5(a_T) & H_5(a_T) \end{bmatrix}. \tag{B22}$$

For $l = 0$, only A_2, B_2 enter, and only the first two rows and columns of (B23) survive. The membrane determinant reduces to

$$\mathcal{D}_0^{\rm mem}(\omega) = J_3'(a_L)H_3(a_L) - J_3(a_L)H_3'(a_L), \tag{B23}$$

whose vanishing determines the fundamental acoustic "breathing" mode. Substituting the definitions (B13), and using the defining equation (A5) to eliminate second and higher derivatives, one may reduce (B23) to

$$\mathcal{D}_0^{\rm mem}(\omega) = \frac{1}{a_L}[(2\mu+\lambda)^2 a_L^2 - 4\mu(2\mu+3\lambda)]W\left[j_0, h_0^{(1)}\right] \tag{B24}$$

in which the Wronskian $W\left[j_l, h_l^{(1)}\right] = j_l(x)h_l^{(1)\prime}(x) - j_l'(x)h_l^{(1)}(x) = i/x^2$ never vanishes. The fundamental breathing mode frequency is therefore given by

$$\omega_0^{\rm mem} = \frac{2}{a}\sqrt{\frac{\mu(2\mu+3\lambda)}{\rho(2\mu+\lambda)}} = \frac{2c_T}{a}\sqrt{3-\left(\frac{2c_T}{c_L}\right)^2}. \tag{B25}$$

Interestingly, this vanishes in the fluid limit $\mu = 0$. This is because a pure fluid membrane can expand or contract, while thinning or thickening to maintain constant volume, at no energy cost.

For large values of l (but not so large that the requirement that the horizontal wavelength $\lambda = 2\pi a/l$ remain larger than the shell thickness, $\lambda/\delta > 1$), the breathing mode should be well approximated by the flat plate acoustic dispersion relation

$$\omega_a = c_0 k,\ c_0 = 2c_T\sqrt{1-(c_T/c_L)^2}, \tag{B26}$$

in which one substitutes $k = l/a$. This is confirmed by the numerical solutions shown in Fig. 1.

For $l \geq 2$, in addition to the acoustic breathing mode, there is also a flexural/bending wave solution. It is perhaps surprising that, as also seen in Fig. 1, the frequency of this mode remains nonzero as $\delta \to 0$. For $\lambda/\delta > 1$, flexural waves on an infinite planar slab have a quadratic dispersion relation

$$\omega_f = D_0 k^2,\ D_0 = \frac{c_0\delta}{2\sqrt{3}} \tag{B27}$$

which vanishes as $\delta \to 0$. This occurs because the only restoring force is due to bending of the membrane, without net stretching, whose energy vanishes with δ.

On a curved surface, however, it is not possible to fully separate bending and stretching degrees of freedom in this way (without tearing the membrane), and this is reflected in the finite mode frequency resulting from (B21). The plane slab result must be recovered for small but finite $k\delta$, in the limit $ka \gg 1$ where the bending energy dominates the curvature-induced stretching energy. The latter scales as $1/a^2$, and is basically independent of k. This limit therefore obtains roughly when $D_0k^2 > c_0/a$, but still $k\delta < 1$, hence $1/\delta > k > 12^{1/4}/\sqrt{a\delta}$. In terms of l, this corresponds to the range

$$a/\delta > l > l_0 \equiv 12^{1/4}\sqrt{a/\delta}. \tag{B28}$$

For $l < l_0$, one predicts that the free mode frequency will be essentially dependent of l (at least for l not too small, so that the mode shape is sensitive mostly to local curvature, rather than the global geometry), while for $a/\delta > l > l_0$ the frequency increases quadratically with k or l. This analysis is confirmed by the numerical results in Fig. 1.

APPENDIX C: SCATTERED FIELD

We consider now the quantitative calculation of the scattered signal from an incident transmitted wave. Of special interest are distinguishable features in the signal due to intrinsic shell resonances.

We consider the specific problem of the elastic shell in a fluid background, with incident wave (B2) therefore specialized to the form

$$\mathbf{s}_{\rm in}(\mathbf{r}) = \sum_{l,m} A_{lm}\mathbf{s}_{L,lm}[j_l(kr)], \tag{C1}$$

where $k = \omega/c$ is the wavenumber in the background fluid with sound speed c, and $\mathbf{s}_{L,lm}$ is defined by (A4) and (A11) (with indices now exhibited explicitly). If the incident acoustic wave is modeled as a simple plane wave in the neighborhood of the sphere, the expansion (B3) leads to coefficients

$$A_{lm} = 4\pi A_0(-i)^l Y_{lm}^*(\theta_T, \phi_T), \tag{C2}$$

in which A_0 is an overall amplitude (see below), and $\theta_T = \pi - \theta'$, $\phi_T = \pi + \phi'$ correspond, for physical convenience, to the direction from the sphere center *towards* the transmitter location (i.e., the direction $-\mathbf{k}$ opposite to the wavevector). Alternatively, if one models the wave as the result of an outgoing spherical wave generated by an isotropic transmitter at point $\mathbf{x}' = \mathbf{x}_T$, the expansion (B4) yields

$$A_{lm} = A_0 k i^{l+1} h_l^{(1)}(kx_T)Y_{lm}^*(\theta_T, \phi_T), \tag{C3}$$

in which θ_T, ϕ_T again correspond to the direction *toward* the transmitter (along $\mathbf{x}_T$). This form follows from the observation that for the scattering problem, with standoff transmitter and origin taken at the center of the sphere, one has $r_< = x$ and $r_> = x_T$. Note that the physical units of A_0 actually differ between (C2) and (C3) (by an inverse length factor) due to the spherical spreading factor in the latter.

The scalar waves (B3) and (B4) represent perturbations in the pressure p or density ρ, and the overall amplitude A_0 is determined by the thermodynamic coefficients relating these to the displacement $\mathbf{s}$: $\delta\rho/\rho = \delta p/\rho c^2 = -\nabla\cdot\mathbf{s}$, where $c^2 = K/\rho$, with $K = \lambda = \rho(\partial p/\partial\rho)_S$ the (adiabatic) bulk modulus. This leads to

$$A_0 = A_\rho/\rho k = A_p/\rho c^2 k, \tag{C4}$$

in which A_ρ and $A_p = A_\rho c^2$ are the physical density or pressure perturbation amplitudes multiplying (B3) or (B4).

Given A_{lm}, using linearity of (B5), the solution for the scattered wave is given by

$$\mathbf{s}_{\rm sc}(\mathbf{r}) = \sum_{l,m} A_{lm}(k) B_{3,l}(k) \mathbf{s}_{L,lm}[h_l^{(1)}(kr)], \tag{C5}$$

where $B_{3,l}$ is the scattering coefficient (which is independent of m) obtained from the solution of (B11)–(B13) (with indices again now exhibited explicitly). The receiver sensitivity is most likely calibrated directly in terms of the pressure wave, for which one obtains

$$\begin{aligned} p_{\rm sc}(\mathbf{r}) &= -\rho c^2 \nabla \cdot \mathbf{s}_{\rm sc} \qquad \text{(C6)} \\ &= \rho c^2 k \sum_{l,m} A_{lm}(k) B_{3,l}(k) h_l^{(1)}(kr) Y_{lm}(\theta,\phi) \\ &= \frac{\rho c^2 k}{4\pi} \sum_l (2l+1) A_l(k) B_{3,l}(k) h_l^{(1)}(kr) P_l[\cos(\gamma)], \end{aligned}$$

in which

$$A_l = A_0 k i^{l+1} h_l^{(1)}(k x_T) \tag{C7}$$

is defined by $A_{lm} = A_l Y_{lm}^*(\theta_T, \phi_T)$. The last line follows from the spherical harmonic addition theorem [10, 11], where $P_l(x)$ is the standard Legendre polynomial, and γ is the relative angle between directions θ_T, ϕ_T and θ, ϕ, i.e., $\cos(\gamma) = -\hat{\mathbf{k}} \cdot \hat{\mathbf{x}}$ for (B3) and (C2), or $\cos(\gamma) = \hat{\mathbf{x}} \cdot \hat{\mathbf{x}}'$ for (B4) and (C3).

[1] S. G. Schock, A. Tellier, J. Wulf, J. Sara and M. Ericksen, "Buried Object Scanning Sonar," IEEE J. Oceanic Eng. **26**, 677–689 (2001).

[2] A. Tesei, A. Maguer, W. L. J. Fox, R. Lim and H. Schmidt, "Measurements and modeling of acoustic scattering from partially and completely buried spherical shells," J. Acoust. Soc. Am. **112**, 1817–1830 (2002).

[3] T. M. Marston, P. L. Marston, and K. Williams, "Scattering resonances, filtering with reversible SAS processing, and applications of quantitative ray theory," IEEE Oceans (2010).

[4] P. B. Weichman, "Validation of Advanced EM Models for UXO Discrimination," Trans. Geosci. Remote Sens. Vol. PP, Issue 99, pp. 1–14 (2013).

[5] See, e.g., presentations by Thomas Bell, Len Pasion, Fridon Shubitidze, and others, in Technial Session 2B the 2011 SERDP-ESTCP Partners in Environmental Technology Symposium: http://symposium2011.serdp-estcp.org/Technical-Sessions/2B.

[6] . The precise acoustic spectral pattern could in principle form the basis for a full physics-based inversion, but this would require an exceedingly large computational overhead, and involve simultaneous determination of a huge number nuisance parameters (especially, knowledge of the sediment background that is generally unavailable). This approach is not necessary.

[7] A. Maguer, E. Bovio, W. L. J. Fox and H. Schmidt, "In situ estimation of sediment sound speed and critical angle," J. Acoust. Soc. Am. **108**, 987–996 (2000). Note that due to its porous nature, sediment acoustic propagation is dispersive at higher frequencies, and the phase speed $c_{\rm sed}(\omega)$ becomes frequency dependent.

[8] A. E. H. Love, *A treatise on the mathematical theory of elasticity* (Dover, 1944).

[9] R. R. Goodman and R. Stern, *Reflection and transmission of sound by elastic spherical shells,* J. Acoust. Soc. Am. **34**, 338 (1962).

[10] J. D. Jackson, *Classical Electrodynamics, 2nd Edition* (John Wiley & Sons, New York, 1975).

[11] E. Merzbacher, *Quantum Mechanics, 2nd Edition* (John Wiley & Sons, New York, 1970).

[12] P. B. Weichman, "T-matrix approach to acoustic multiple scattering from an array of compact targets in a layered medium," BAE Systems Technical Report to SERDP (2011).

[13] P. B. Weichman, I. Ekhaus, Y.-S. Lai, and E. M. Lavely, "A bistatic acoustic scattering approach to improved buried underwater target discrimination," BAE Systems Technical Report to SERDP (2012).

[14] A. Maguer, E. Bovio, W. L. J. Fox and H. Schmidt, "*In situ* estimation of sediment sound speed and critical angle," J. Acoust. Soc. Am. **108**, 987–996 (2000).

[15] K. L. Williams, D. R. Jackson, E. I. Thorsos, D. Tang, and S. G. Schock, "Comparison of Sound Speed and Attenuation Measured in a Sandy Sediment to Predictions Based on the Biot Theory of Porous Media," IEEE J. Oceanic Eng. **27**, 413–428 (2002).

[16] Direct measurement of sediment sound speed in Shallow Water '06," J. Yang, D. Tang, and K. L. Williams, J. Acoust. Soc. Am. **124**, EL 116–121 (2008). DOI: 10.1121/1.296303

[17] P. B. Weichman, E. M. Lavely, E. H. Hill III, and P. D. Zemany, "Through-the-wall microwave building tomography, Chap. 7 in *Through-the-Wall Radar Imaging*, M. Amin, Editor (CRC Press, 2011).